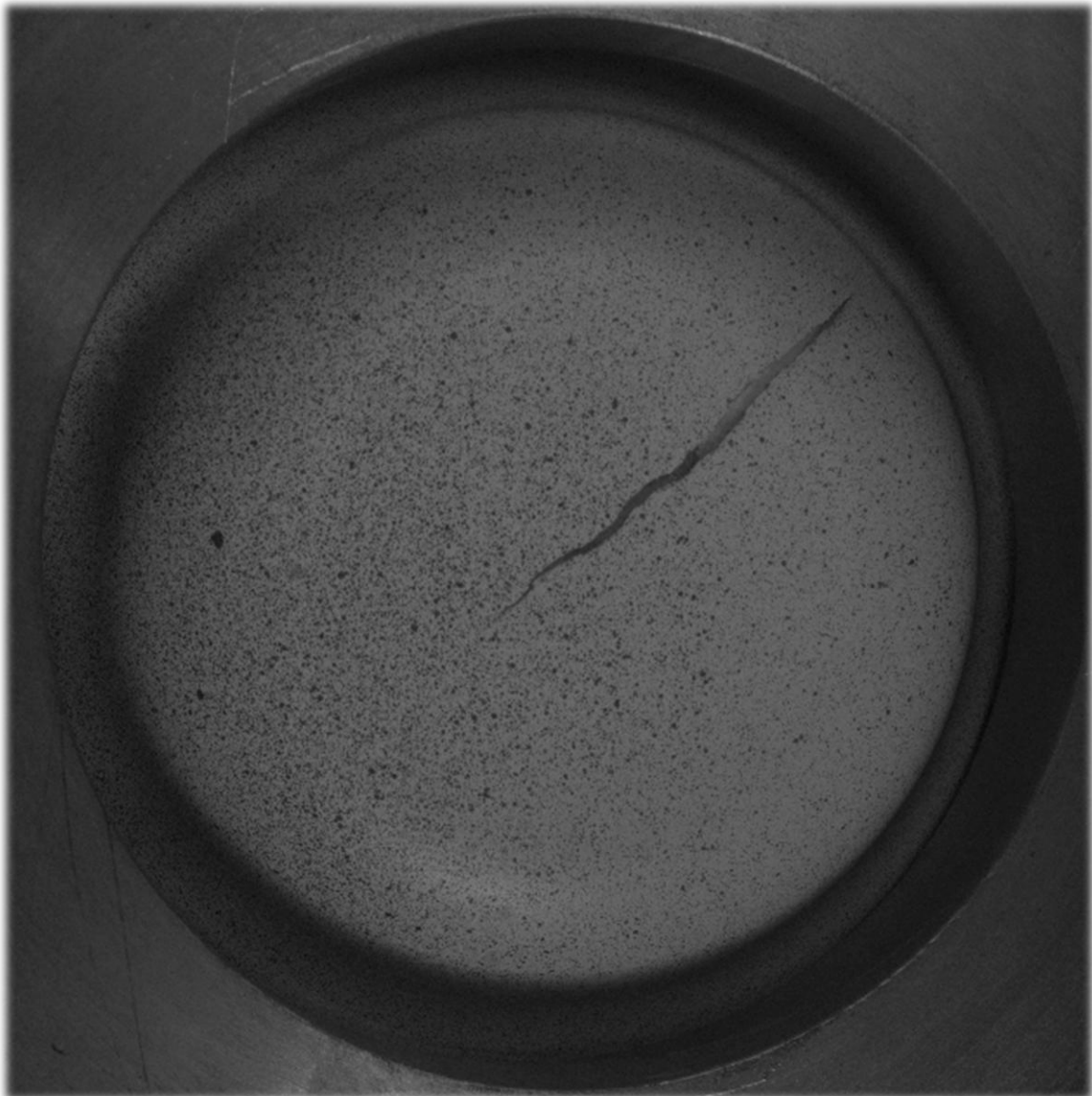


Thesis

Failure behavior of steel under various combinations of biaxial stress

By

Robin Buijs



Thesis

Failure behavior of steel under various combinations of biaxial stress

By

Robin Buijs

in partial fulfillment of the requirements for the degree of

Master of Science

in Offshore & Dredging Engineering

at the Delft University of Technology

Supervisors: Dr. C. L. Walters
M. A. Adly, Ph.D. Candidate
Thesis committee: Dr.ir. P. de Vos

Thesis for the degree of MSc in Offshore & Dredging Engineering in the specialization
of Structural Design and Analyses

Failure behavior of steel under various combinations of biaxial stress

By
Robin Buijs

This thesis (MT.24/25.025.M) is classified as confidential in accordance
with the general conditions for projects performed by the TUDelft.

Date of Exam
29-01-2025

Thesis exam committee

Chair/Responsible Professor: Dr. C. L. Walters

Staff Member: M. A. Adly

Staff Member: Dr.ir. P. de Vos

Abstract

Understanding the failure behavior of thin-walled steel structures under large-deformation plasticity and fracture is crucial for assessment of accidental loading conditions. This thesis will experimentally determine the crack propagation direction in a thin steel sheet under different combinations of in-plane strain, which is essential for improving simulations. Necking and crack angles in a commercially available ductile steel sheet (DC01) are determined under various stress conditions, ranging from uniaxial to equi-biaxial tension. A state-of-the-art formability testing method (Marciniak) is adapted to meet the specific needs of this project. Through tensile testing, the Lankford Parameters of DC01 steel are determined, with which a theoretical assumption of the crack angle can be made using Hill's theory (1952). By varying the specimen and carrier dimensions, the strain ratio range of $-\frac{1}{2}$ to near 1 is tested. A Digital Image Correlation (DIC) system is used to measure deformations and strains during the whole deforming process. Pictures taken from the DIC system and post-mortem section cuts allow for the determination of the crack angle with respect to the in-plane and through-thickness directions. The resulting crack angles agree with the theoretical angles determined by Hill (1952) when the frame of reference of determining the crack angles are rotated.

Acknowledgments

I would like to thank Dr. C. L. Walters and M. Adly for taking the time and for their feedback, patience, and provided knowledge. I would like to thank T. Veer for his feedback and expertise. I would also like to thank my family, especially my mom, for their patience and support.

Contents

1	Introduction	7
2	Background Information	8
2.1	Forming Limit Diagram	8
2.2	The Lankford Parameters.....	9
3	State Of The Art	10
3.1	The Current Testing Methods.....	10
3.2	The Relevant Stress States.....	13
3.3	The Crack Direction	14
3.4	Boundary Condition.....	15
4	Methodology.....	16
4.1	The Designed Marciniak Test.....	16
4.2	Tensile Testing.....	18
4.3	Marciniak Testing.....	18
5	Results	22
6	Discussion.....	30
7	Conclusion	32
	Bibliography	33
	Appendix	36

1 Introduction

Ship structures are subjected to a wide variety of loading conditions. To better understand the limit states and behavior of those structures during extreme loading, it is necessary to understand the failure behavior of metals under different stress states. A variety of unique tests are available to apply different stress states to metals. The main user of those tests is the automotive industry for determining the formability of a material. Due to the rise in demand for cars in the last century, there has been a rapid development of formability tests. This development was mostly focused on the onset of the necking in sheet metals. Making use of the state of the art of formability tests, a test could be designed for structural assessment purposes that go until fracture.

Assessment for extreme loading, such as salvage, crash, and survivability, requires a correct simulation of crack initiation and propagation. Simulation of crack initiation requires an understanding of the orientation of the crack along with the behavior as it opens. While this has been studied numerically and analytically, it requires additional experimental study for more accurate future FEA simulations and assessments of salvageability and survivability (Heidari & Walters, 2020). The crack propagation has to date not been experimentally determined for ship steel metals.

The crack propagation can be affected by the anisotropy properties of a material, and when determining the crack propagation two failure modes are important (Yu et al., 2022). One failure mode occurs when the onset of necking happens before fracture, and the resulting angle is called the necking angle. The other failure mode is where fracture happens without the onset of necking, and this resulting angle is called the fracture angle. The necking angle differs from the fracture angle for most biaxial stress states. Therefore, the importance of the onset of necking and the effect of anisotropy on the crack propagation underscores the need for experimentally testing with ship steel metals. This thesis aids in validating and possibly expanding the theoretical knowledge about crack propagation, shows the limitations of the testing methods, and provides the results for the following research question:

What is the crack propagation direction for an anisotropic rolled steel for the uni-axial till equi-biaxial tension stress states? And how does this compare with the expected crack angles?

The progress of this thesis report approximately follows the structure of the project. This thesis starts with background information. Secondly, a short review of the state of the art of formability testing methods, and crack propagation is given. A test is designed. The results of experimenting are given and are analyzed. Finally, the results are discussed, and conclusions along with further recommendations are provided.

2 Background information

This section will introduce key concepts for understanding this thesis. The Forming Limit Diagram (FLD) is first introduced, followed by the Lankford parameters.

2.1 Forming Limit Diagram

In the sheet metal forming industry, a Forming Limit Diagram (FLD) is used to determine the safe and critical deformation limits during plastic deformation. The FLD is a plot with the major strain, ε_1 , along the y-axis and the minor strain, ε_2 , along the x-axis. Through experimental testing, the FLD can be obtained from a sheet metal specimen. The specimen is deformed until it necks for the necking limit, and until it fractures for the fracture limit. Those limits are the strains that are measured, plotted into the FLD. Testing this for different strain ratios of $(\frac{\varepsilon_2}{\varepsilon_1})$ can create a Forming Limit Curve (FLC).

The strain ratio $(\frac{\varepsilon_2}{\varepsilon_1})$ is called the ρ – ratio. Deformations that result in strains below the FLC are safe, and the points above the FLC are where necking or fracture will occur, depending on the chosen critical limit. The FLD can also help to determine if the onset of necking happens before or after fracture for different strain ratios. On the left of Figure 2.1, a Forming Limit Diagram is shown with the Fracture Forming Limit Curve (FFLC) in red and the Forming Limit Curve shown in blue. The relative position of the FFLC to the FLD is different for each material. In this particular Forming Limit Diagram, necking will occur before fracture for the strain ratios near zero. Fracture without the onset of necking will occur at the higher strain ratios on the far right and left in this example.

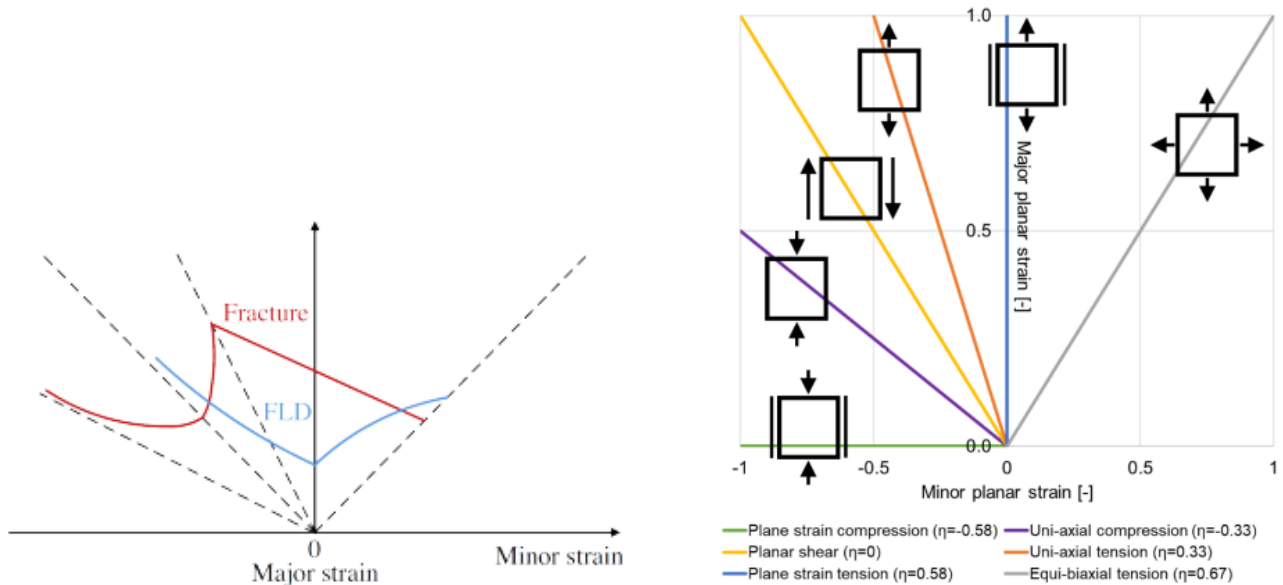


Figure 2.1: A Forming Limit Diagram (FLD), with the Fracture Forming Limit Curve in red (Chung et al., 2014) (Left) and various important biaxial stress states are presented in the major planar strain and the minor planar strain with their respective triaxiality (Coppejans & Werter, 2022) (Right).

Assuming constant strain paths, each strain ratio results in a different biaxial stress state, and vice versa. Each biaxial stress state can also be represented by the stress triaxiality η . On the right of Figure 2.1, some important biaxial stress states with their stress triaxialities are shown. When linking the strain ratio to a stress triaxiality, the out-of-plane stress, σ_3 is assumed to be zero. Stress triaxiality is the ratio of the mean stress σ_{mean} and the von Mises equivalent stress σ_v . The stress triaxiality ratio is shown in equations 1:

$$\sigma_{mean} = \frac{\sigma_1 + \sigma_2 + \sigma_3}{3}$$

$$\sigma_v = \sqrt{\frac{(\sigma_1 - \sigma_2)^2 + (\sigma_2 - \sigma_3)^2 + (\sigma_3 - \sigma_1)^2}{2}}$$

$$\sigma_3 = 0$$

$$\eta = \frac{\sigma_{mean}}{\sigma_v} \quad (1)$$

2.2 Lankford Parameters

Often, sheet metals are anisotropic due to the sheet metal production methods (Banabic et al., 2000). The Lankford parameters quantify the anisotropy of a material's plastic deformation behavior. The Lankford parameters are the ratios of the width strain to the thickness strain when tensile tests are performed in different directions relative to the rolling direction. Often, they are measured in the 0° , 45° and 90° to the rolling direction and denoted respectively as r_0 , r_{45} and r_{90} . The Lankford parameters are determined between the 15 to 20% of the length strain (Worldautosteel, 2021).

3 State of the art

This chapter contains the state of the art regarding the formability tests and crack propagation. The relevant stress states for this thesis are explained, and the requirements for this research are provided.

3.1 The current testing methods

Although there are a lot of formability tests available, in this chapter, the most promising are shown: The hydraulic bulge test, the Nakajima test, and the Marciniak test.

In a hydraulic bulge test, a test specimen and carrier sheet are clamped between a circular die and a circular blank holder. Pressure is applied on the bottom of the carrier sheet to deform the test specimen until necking and/or fracture. Banabic et al (2013) proposed an improved hydraulic bulge test. This improved test could cover not only the positive but also the negative sides of the FLD. In Figure 3.1, a schematic view of the improved hydraulic bulge test is shown. By adding holes in the test specimen at specific locations, a wider range of the FLD can be determined. The effect of the specimen geometry on the strain ratio will be further explained in this chapter. The publication of Banabic et al (2013) lists the simplicity of the laboratory equipment as an advantage. A disadvantage of the hydraulic bulge test is the out-of-plane deforming of the test specimen. The improved hydraulic bulge test also lacks verification if this test setup works for all the relevant biaxial stress states. For example, no specific carrier hole dimensions are given, thus verified, to achieve the uni-axial tension strain ratio. (Banabic et al., 2013).

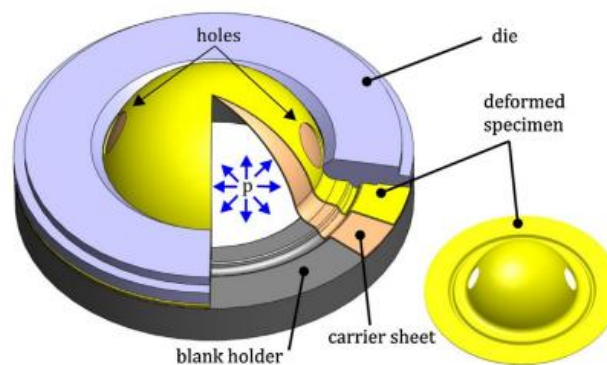


Figure 3.1: A schematic view of the improved Hydraulic bulge test (Banabic et al., 2013).

In Figure 3.2, a schematic view of both the Nakajima test (left) and the improved Marciniak test (right) with their formed samples are shown (Chen & Fang, 2018). In the conventional Nakajima test, the test specimen is clamped between a circular die and a circular blank holder while a hemispherical punch applies a load in the middle. By progressively increasing the displacement, the specimen will start deforming until necking and/or fracture. The Nakajima test is comparable to the Marciniak test. The Marciniak test makes use of a hollow flat punch, which instead acts on a carrier blank with a circular hole in it. This results in an in-plane deformation compared to an out-of-plane deformation by the Nakajima test, which makes the strain path linear. The curvature of the deformation with the Nakajima test will decrease the accuracy of the test due to a possible non-linear strain path. Figure 3.3 shows the occurrence of the non-linear strain path in the Nakajima test. Both methods are recommended by a specialized International Deep Drawing Research Group (IDDRG) for determining the FLC (Banabic et al., 2013). The Nakajima test is deemed to be easier to use, mostly due to the lack of the carrier sheet (Raghavan, 1995; Chen & Fang, 2018). The studies also noted the disadvantages of the Nakajima test: The accuracy loss due to the non-linear strain path and the possibility of wrinkling. Also in the Nakajima test, the lubrication condition needs to be further improved according to Chen & Fang (2018). They found inadequate use of lubricant would cause the fracture to occur away from the pole of the gage section, therefore unusable for the determination of the FLC. Also, the out-of-plane deformation can make the crack angle determinations more difficult to determine.

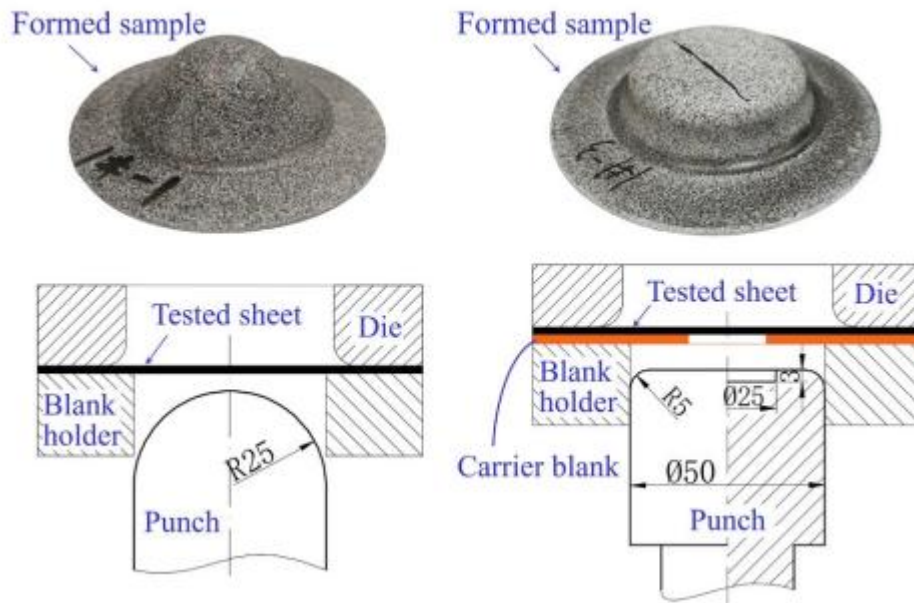


Figure 3.2: A schematic view of the Nakajima test (left) and the improved Marciniak test (right) (Chen & Fang, 2018).

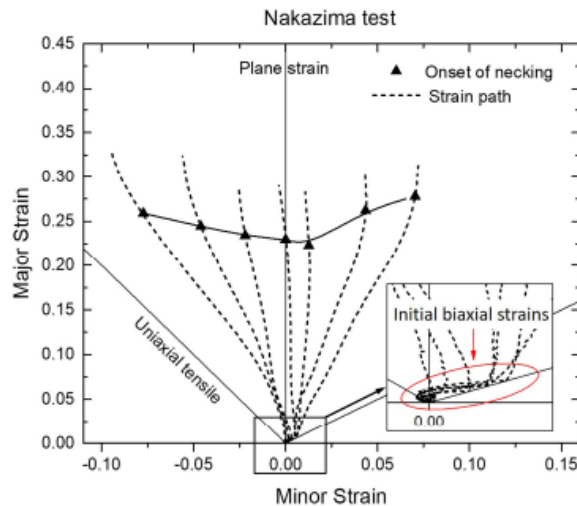


Figure 3.3: An FLD that highlights the non-linear strain paths produced by the Nakajima test (Chen & Fang, 2018).

Research has been done to improve the accuracy of the Nakajima test and improve the useability of the Marciniak test. Chen & Fang (2018) proposed an extensive theoretical correction algorithm in the post-processing to correct the non-linear strain paths, and make the results of the Nakajima test similar to the Marciniak test.

Deng & McGuire (2018) combined both tests by changing the punch. In Figure 3.4, the modified punch geometry is shown. It aims to keep the simplicity of the Nakajima test and the linear strain path of the Marciniak test without the carrier blank. The flathead on top with a groove is for a frictionless and in-plane result. The groove and the curvature of the punch ensure failure in the central region without the need for a carrier blank. The combined test has been validated by numerical analyses. While the modified punch geometry looks promising due to the lack of a carrier blank, the test hasn't been experimentally validated. No data is given on the test specimen dimensions to achieve the different stress states with this new punch design.

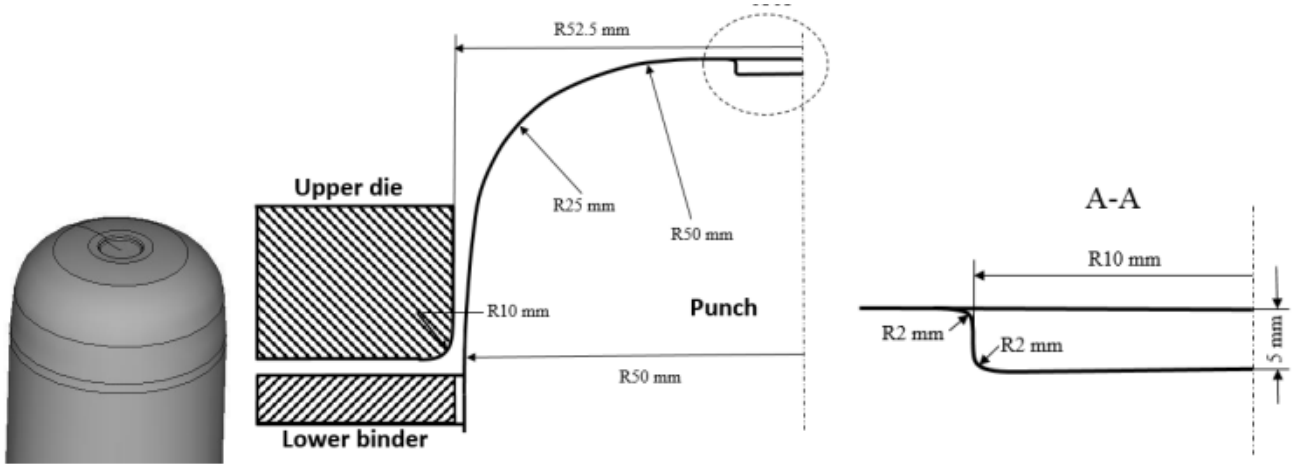


Figure 3.4: The Nakajima and the Marciniak test combined punch geometry (left), a schematic view with the dimensions of the punch (middle) and the local dimensions of the top groove (right) (Deng & McGuire, 2018)

A more validated test is the modified Marciniak of the publication of Bong et al (2012). In Figure 3.5, a schematic view of the modified Marciniak is shown. The carrier blank and test specimen are kept in place by a lockhead. Note that the word washer is the same as a carrier blank.

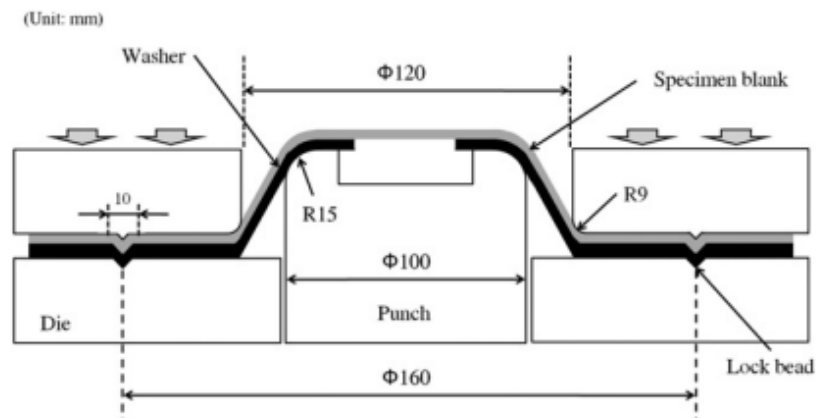


Figure 3.5: A schematic view of the modified Marciniak test with the dimensions (Bong et al., 2012).

The groove in the punch along with the modified carrier blank ensures failure in the central region. The groove and the holes in the carrier blanks ensure the free expansion of the test specimen. A schematic view of the material flow is shown on the left of Figure 3.6. The punch moves up, causing the carrier blank and the test specimen to move outwards. By applying a lubricant between the punch and the carrier blank, but not between the carrier blank and the test specimen, an additional friction force at the test specimen will be generated. A strain concentration is created in the center region. Raghavan (1995) proposed a new Marciniak test method in which only the test specimen and the carriers are varied. The study introduced combinations of test specimen geometry and carrier geometry with which a wide range of the FLD can be determined. This proposed method with a single punch and die geometry has since been used in multiple other publications, for example in the publications of Bong et al (2012) and Moshksar & Mansorzadeh (2003). In Figure 3.6, some of the geometries and combinations of carrier and test specimen are shown on the right. Raghavan (1995) has categorized the combinations into 4 categories for convenience. These categories have different dimensions for the test specimen width, notch radius, and carrier hole diameters, and can be applied to obtain different strain ratios. Type 1 is for the strain ratios of $(\frac{\epsilon_2}{\epsilon_1}) < 0$. The small width of the specimen ensures a uniaxial strain and a stress localization in the center, so no carrier is needed. Type 2 is for the strain ratios of $(\frac{\epsilon_2}{\epsilon_1}) \sim 0$. The width is increased, and the specimen has become rectangular. The small width of the specimen still constrains deformation in the width direction, resulting in failure near the plain strain ratio. Type 3 is for the strain ratios of $(\frac{\epsilon_2}{\epsilon_1}) > 0$. Here, the notch radius on the sides limits the stretching in the width direction, resulting in intermediated biaxial strain. Type 4 is for the strain ratios of $(\frac{\epsilon_2}{\epsilon_1}) \sim 1$. Now, the specimen is square instead of more rectangular, resulting in equi-biaxial strain. Apart from Type 1, the carrier ensures failure in the central zone of the specimen. The study noted that the carrier material should have a higher formability than the test specimen used for it to work. The rolling direction according to the ISO standard is in the width direction (ISO-12004-2, 2021).

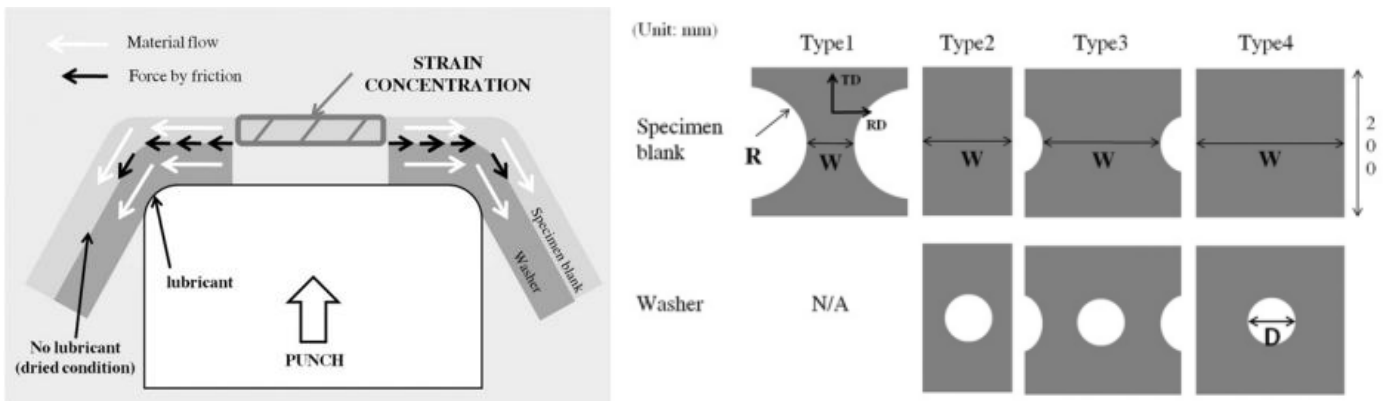


Figure 3.6: A schematic view of the material flow in a Marciniak test (left) and some combinations of carrier and test specimen for the different types of strain ratios (right) (Bong et al., 2012).

3.2 The relevant stress states

There is not one testing method that could provide a testing setup that could cover the whole range of biaxial stress states. Therefore the focus of this project is on the most relevant stress states. Research has been done by Coppejans & Werter (2022) and Atli-Veltin et al (2016) on the most relevant stress states during a collision of ships. In the publication of Coppejans & Werter (2022) the plots of Figure 3.7 are generated from simulations of a collision of ships using FEA without failure criteria to find the energy dissipation per stress state for different indentations. As seen in Figure 3.7, at the first impact, the stress states near equi-biaxial tension (triaxiality $\frac{2}{3}$) are critical, and for a greater indentation, the impact of near uniaxial tension stress states (triaxiality $\frac{1}{3}$) are also critical. Therefore, the most relevant stress states and thus the focus of this project are near uniaxial tension and equi-biaxial tension. Both publications agree on the importance of the stress state range near pure shear (triaxiality 0). Atli-Veltin et al (2016) highlighted that the compression states (triaxiality $-\frac{2}{3}$ to 0) can't be neglected as well. These stress states fall out of the scope of formability testing methods that focus primarily on the uniaxial and equi-biaxial stress states. In a ship structure, uni-axial stress typically occurs in structures subjected to axial loadings, for example the longitudinal stiffeners. Plane and equi-biaxial stresses occur typically in 2D plates, for example in the skinplates inbetween the stiffeners (Rigo & Rizzuto, 2003).

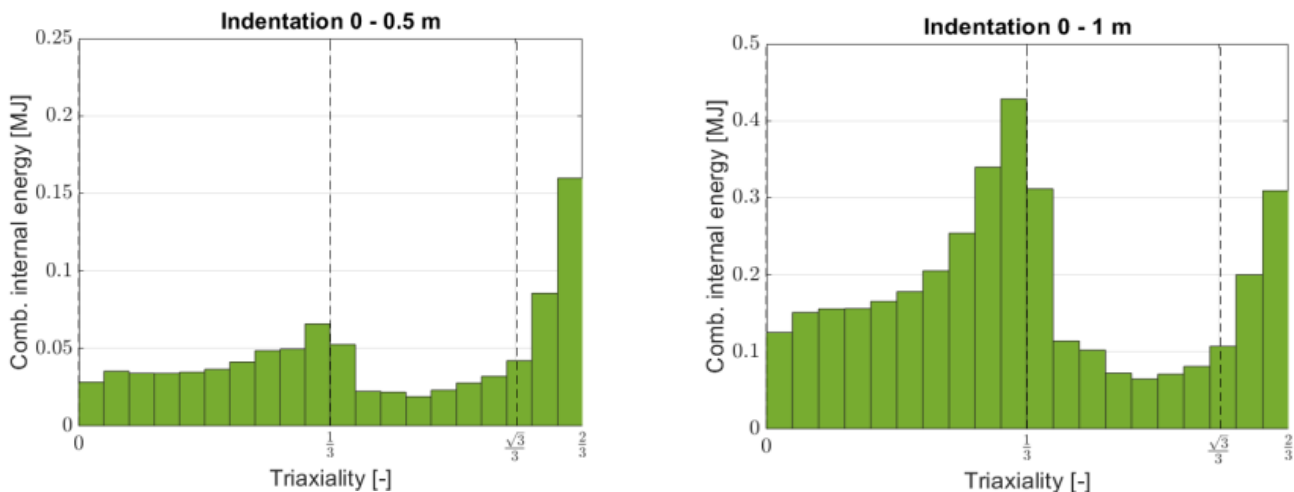


Figure 3.7: The plastic energy absorbed in various tension-based stress states for different indentations (Coppejans & Werter, 2022).

3.3 The crack direction

For each stress state the crack direction needs to be determined. When determining the crack direction, two failure modes are important. Fracture after the onset of necking, and fracture without the onset of necking. The crack angle can therefore be categorized by respectively the necking angle and the fracture angle. For the latter, Bai & Wierzbicki (2010) used the Mohr-Coulomb fracture criterion to find the fracture direction for different biaxial stress states. They found the fracture angle remains perpendicular to the first principal stress except for the domain between pure shear and uniaxial tension for the tension states. According to the Mohr-Coulomb criterion, for the relevant biaxial stress states the fracture angle is zero relative to the second principal stress. The FLD theory mostly focuses on the onset of necking, but it also gives an insight into the necking direction. Hill (1952) has offered a simple estimation of the necking angle for the left side of the FLD:

$$\theta = \arctan \left(\sqrt{-\frac{\varepsilon_2}{\varepsilon_1}} \right) \quad \text{for} \quad -\frac{1}{2} \leq \frac{\varepsilon_2}{\varepsilon_1} < 0 \quad (2)$$

The necking angle of the right side of the FLD is assumed to be in a perpendicular direction to the major strain, so an angle of zero (Hutchinson & Neale, 1978). This, and equation 2 have been verified for aluminum alloy steel by Yu et al (2022). In Figure 3.8, the results of the fracture angles they found using the Nakajima test are plotted against the strain ratios together with the theoretical necking angle of Hill (1952). The results align well, only near equi-biaxial the crack angle seems to be disunited. This can be explained by the other aspects that affect the necking angle.

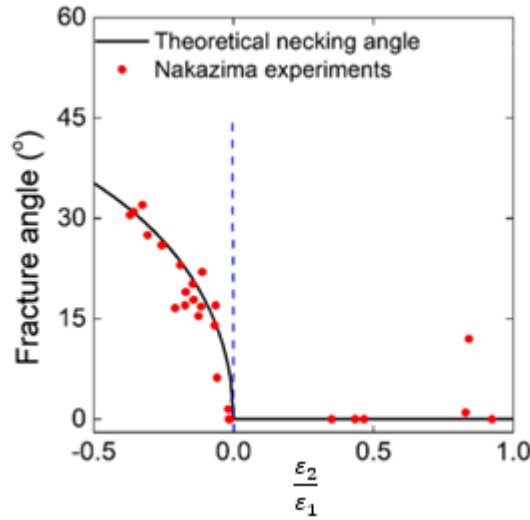


Figure 3.8: The fracture angles for different strain ratios found using the Nakajima test are plotted with the theoretical necking angle (Yu et al., 2022).

Yu et al (2022) and Dasappa et al (2012) found that along the onset of necking, also the material anisotropy and the general yield surface affect the necking angle, thus the crack propagation. The Lankford parameter can be used to quantify the anisotropy. Dasappa et al (2012) looked into the Lankford parameters effect on the necking angle, and found that the Lankford parameters have an effect on the necking angle, but also on the strain ratio onset of the necking angle. When the r_{45} is less than or equal to the r_0 and r_{90} of a material, a necking angle of zero is expected, so perpendicular to the first principal stress. The exception is when r_{90} is considerably higher than the rest. Then, the necking angle will change to 90° for strain ratios near equi-biaxial. When the r_{45} is greater than or equal to either the r_0 or r_{90} of a material a non-zero necking angle is expected. The difference between the r_{45} and the other r -values determines at which strain ratio the onset of the necking angle is. A bigger difference means the onset of the necking angle will be at a lower strain ratio. After the onset of necking, the necking angle will increase to 45° near the equi-biaxial strain ratio, even if the r_{90} is considerably higher. Yu et al (2022) verified the effect of the anisotropy of a material with two aluminum sheets. One of the aluminum sheets has a strong anisotropy with the r -values of $r_0 = 0.83, r_{45} = 0.60$ and $r_{90} = 0.93$. For equi-biaxial strain the necking angle went to 90°. The onset of the necking angle was almost near the equi-biaxial strain ratio, because of the low difference between either the r_0 or r_{90} values with the r_{45} value. The other aluminum sheet with a strong anisotropy has the r -values of $r_0 = 0.38, r_{45} = 0.84$ and $r_{90} = 1.13$. For equi-biaxial strain, the necking angle went to 45°. The onset of the necking angle happened at a lower strain ratio. because of the high difference between the r_0 and the r_{45} values. The experimental tests of Yu et al (2022) agree with the theory of anisotropy.

Dasappa et al (2012) also studied the effect of the yield surface of a material on the necking angle by varying the equibiaxial yield strength in their simulations. The study found that an increased yield strength will result in the onset of necking to start for lower strain ratios. In Figure 3.9, the effect of the yield surface on the onset of the necking angle can be seen. The necking angle ranges from 0° to 50°, depending on ρ and material. The theory could differ slightly as Walters and Heidari (2020) mention the effect of ignoring the plastic anisotropy, material inhomogeneity and triaxial stress state in the theory proposed by Hill (1952).

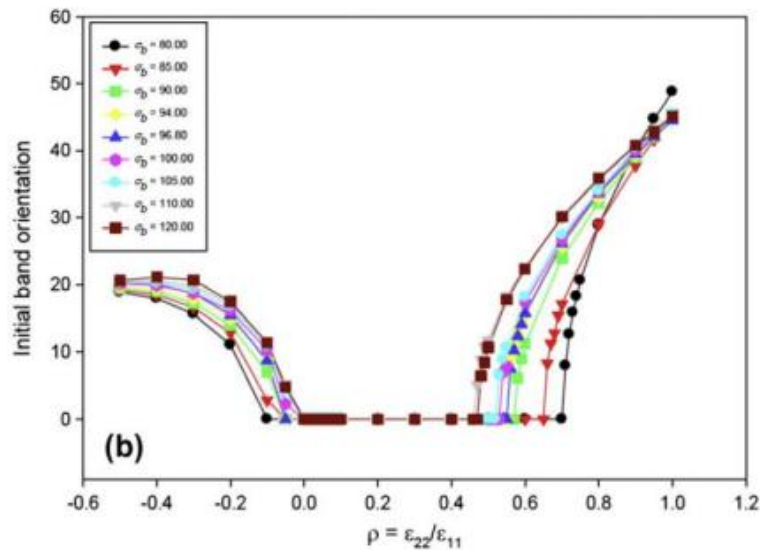


Figure 3.9: The effect of different biaxial yield surfaces on the fracture angle (initial band orientation) for different strain ratios (Dasappa et al., 2012).

With the use of the Nakajima test is for aluminum sheet metal the crack angle determined. (Yu et al., 2022) No experimental research has been done on the crack angle for steel sheet material. Steel has already been put in multiple papers in a formability test setup to research its formability. In this research the point of necking was important. This thesis focuses on going further than necking and looks into the crack behavior when failing. By determining the crack angle for steel sheet material the theory can be checked for steel. This thesis aids in filling that knowledge gap.

3.4 Boundary conditions

Various testing methods for evaluating sheet metal formability have been developed, but there is not one favorite testing method. Each test could be tailored to specific needs. For the goal of this thesis, a few specific requirements are made that restrict the scan of the state of the art for suitable methods that conform to these boundary conditions:

- Due to the small timeframe of a thesis, this project is limited to one test setup.
- The test setup should adhere to the machine capabilities available for this project. This project is limited to machines available to the TU Delft.
- The test setup should be within a reasonable price range for a thesis project on the TU Delft.
- The test should have the scope of strain ratio -0.5 to 1.0 .
- The test should be able to deform a cold rolled steel until fracture.

The testing method that suits the boundary conditions listed above should be able to measure the crack direction sufficiently. The measured crack direction should not be influenced, therefore some more requirements are used:

- The stress state should be as constant as possible in the gage section.
- Failure should occur in the gage section.
- The gage section of the test should be as large as possible, and throughout the gage section, the stress/strain field should be as even as possible with an even thickness.
- The gage section should be measurable with measurement devices (DIC). This means the gage section should be visible throughout the whole operation.

4 Methodology

The Marciniak testing method is used to determine the crack angle for steel sheet material. The Marciniak test is a widely verified deforming testing method and meets the listed boundary conditions of Chapter 3.4. Other testing methods like the Nakajima testing method can also be used like by Yu et al.(2022). The advantage of the Marciniak testing method over the Nakajima testing method is the in-plane deformation of the test specimen. This significantly eases the crack angle determination during the post-processing. This project's design of the Marciniak testing method is guided by the state of the art of the Marciniak test. In Figure 4.1, the full design of this projects Marciniak test is shown.

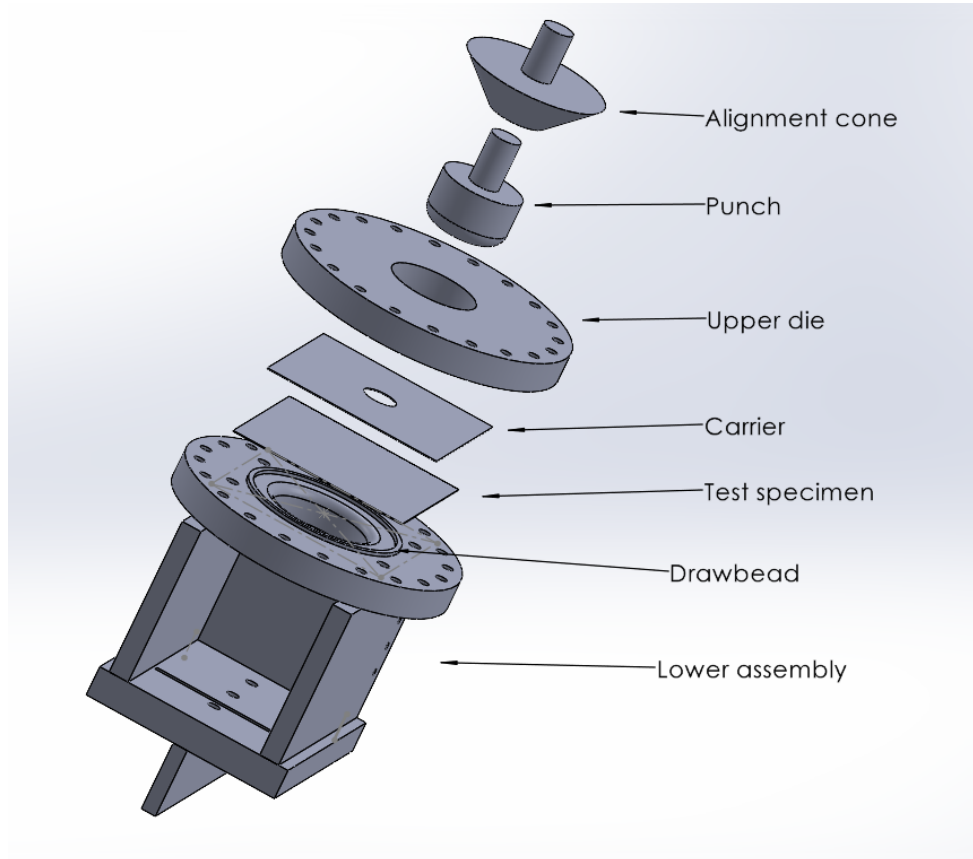


Figure 4.1: The full design of this projects Marciniak test shown in Solidworks.

4.1 The designed Marciniak test

The primary means to answer the research question is to develop a working test setup that can test the most relevant stress states. This will be done by adhering to the state of the art Marciniak tests as much as possible while keeping the forces in the whole setup as low as possible. Too high forces like the punch force and clamping force can prove to be critical. The dimensions of the core of the Marciniak testing method are kept roughly the same as in the publications of Bong et al. (2012) and Raghavan (1995). These dimensions of the combination of the punch and the test specimen and carrier are already validated, and only slight adjustments are needed. Both the test specimen and the carrier sheets are made of the same DC01 steel. The test specimen will have a thickness of 1 mm . The carrier will have a higher thickness of 1.25 mm as according to Tisza & Kovács (2012) the slightly higher sheet thickness will increase deformability.

To ensure the sheets will not move along with the punch, a drawbead is used, as seen in Figure 4.2. The dimensions of the specimen and carrier sheets are dependent on the punch diameter and the drawbead location. The sheets will deform over the drawbead when clamping the dies together, thus preventing them from drawing in and affecting the failure conditions that are being researched in this project. Other than the Type 4 sheets, the Types 3 to 1 have some sides not clamped by the drawbead. This is required to achieve the different stress states as explained earlier in Chapter 3.2.



Figure 4.2: The drawbead design in the upper and lower die shown in Solidworks.

One of the conditions of this project is that the gage section of the test specimen is visible during the testing process. This will be done by placing a first-surface mirror at an angle of 45° below the test specimen. A 3D-printed base for the first-surface mirror is used to keep the mirror at an angle of 45° for all the tests, as can be seen in Figure 4.3. By using a first-surface mirror, the image will be clearer than a normal mirror, due to its single image reflection.

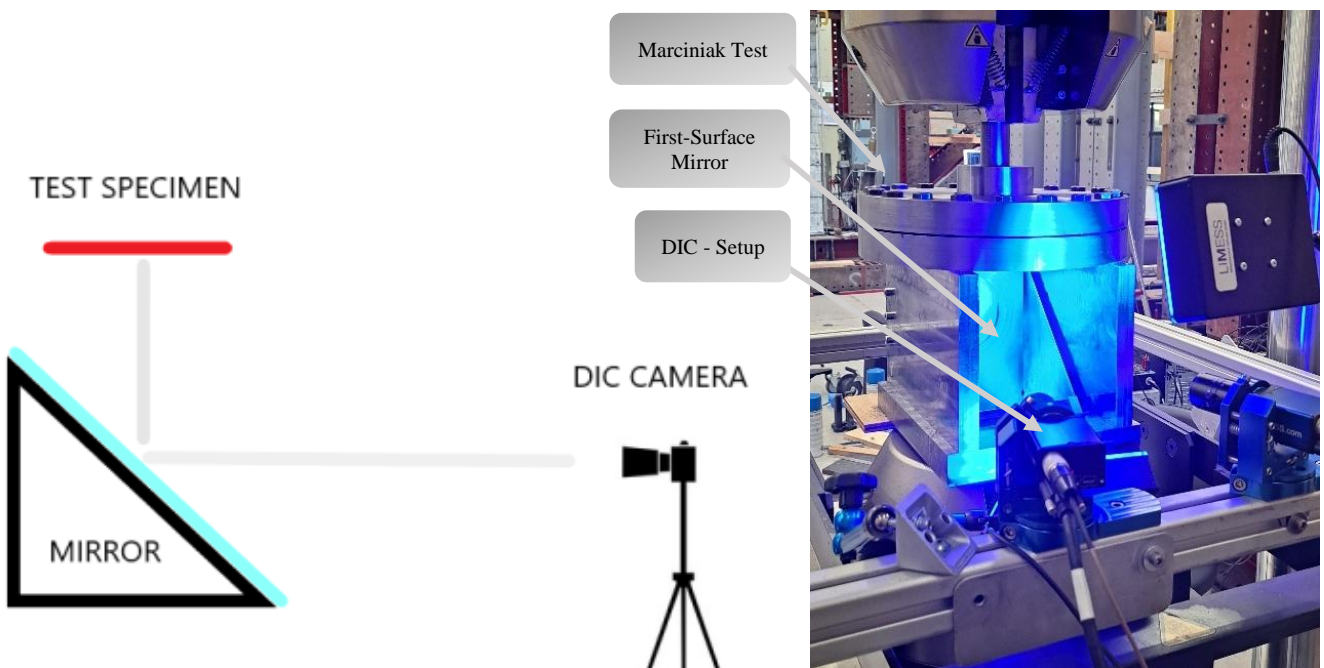


Figure 4.3: A schematic view of the camera setup (left) and the real camera setup in the lab (right).

The mirror should be big enough to see the whole gage section through the lower die entry of 96 mm . With a mirror of 205 mm the height and length of the mirror holder is 145 mm to acquire the 45° angle. By adding a clearance gap for the punch to move without touching the mirror, the height of the vertical walls will be taken as 160 mm . With a thickness of 20 mm , the vertical walls can accommodate M6 crews, and there is room for alignment purposes if necessary. A vertical back wall of the same height and a length of 139.8 mm is added for extra strength between the vertical walls. The thickness of the vertical back wall is 15 mm , as here the alignment can be done by moving the whole setup within the vertical clamping system.

4.2 Tensile testing

The properties of the testing material should be determined to get the Lankford Parameters, and this is done by tensile testing. The testing material for both the test specimen and the carrier is DC01 steel. For the tensile tests, three orientations with respect to the rolling direction are tested: 0°, 45°, and 90°. The flat specimen standard ASTM E8 design is used (*ASTM E8*, n.d.). The tensile tests are performed in an Instron 8854 axial-torsion test machine, and 2 DIC cameras are used for determining the strains. The DIC software of Istra 4D is used (*Istra 4D*, 2019). A speckle pattern is applied on the test specimen to be able to measure the displacements on the testing material. First, the gage length of the test specimen is spray painted white for better contrast and limiting the reflection of the material. A black speckle pattern is applied by spray painting over the test specimen from the side. A rule of thumb for using the right speckle pattern is that one speckle should be around 3 to 5 pixels, and every facet in the DIC software should contain 3 to 10 significant speckles. The DIC cameras will be positioned as close as possible to the test specimen, while also maintaining a good focus using the focus rings of the DIC cameras. The strain is determined during post-processing of the DIC results. With the DIC, the length strain and the width strain can be determined with the reference points shown in Figure 4.4. This will be called the coordinate process. Due to the uncertainty of the place of the specimen in the reference plane, the coordinates are used instead of the displacements from the DIC software itself. The coordinates can be used in Equations 3 to calculate the length strain and the width strain.

$$\begin{aligned}
 L_{Length} &= \sqrt{(x_2 - x_1)^2 + (y_2 - y_1)^2 + (z_2 - z_1)^2} \\
 L_{Width} &= \sqrt{(x_4 - x_3)^2 + (y_4 - y_3)^2 + (z_4 - z_3)^2} \\
 \epsilon_L &= \frac{L_L - L_{L0}}{L_{L0}} \\
 \epsilon_w &= \frac{L_w - L_{w0}}{L_{w0}} \\
 \epsilon_{L-true} &= \ln(1 + \epsilon_L) \\
 \epsilon_{w-true} &= \ln(1 + \epsilon_w)
 \end{aligned} \tag{3}$$

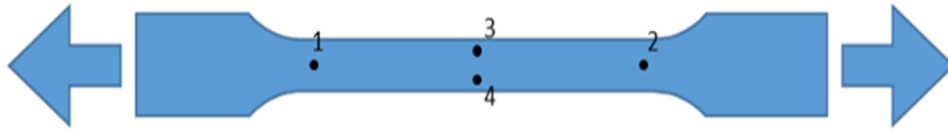


Figure 4.4: A schematic view of the tensile specimen with the reference points for the DIC software.

Again, due to the uncertainty of the place of the specimen in the reference plane and simply due to the small margins of the thickness strain, the thickness strain will be calculated by the use of conservation of volume. Equation 4 can be used to determine the thickness strain:

$$\epsilon_{t-true} = -\epsilon_{L-true} - \epsilon_{w-true} \tag{4}$$

The ratio of the width strain over the thickness strain is the Lankford parameter. The Lankford parameter can be found by taking the slope of the thickness strain versus width strain plot at around 15% and 20% strain (Worldautosteel, 2021).

4.3 Marciniak testing

The crack direction can be estimated using the Lankford Parameters derived from tensile testing. To verify this estimation, Marciniak testing is conducted on steel specimens. When setting up the Marciniak test on the Instron machine, an alignment cone is used to ensure the die is centered along the gripper axis. Once alignment is complete and the lower assembly is securely clamped, the alignment cone is replaced with the punch. With the entire setup in place, the DIC system can be applied, similar to the procedure in tensile testing. During the Marciniak test, the specimen deforms towards the mirror and, consequently, towards the DIC cameras. This deformation requires a higher depth of

field compared to tensile testing. To achieve this, a smaller aperture is used on the cameras. However, a smaller aperture reduces the brightness of the image, so the shutter speed is increased to 1 ms, and additional light is directed at the specimen to compensate. If the shutter speed is set too high, the images can become blurry due to movement of the specimen. Dummy tests are used to verify the lighting setup throughout the test. After a trial-and-error process, two lights are positioned to evenly illuminate the entire gage section during deformation.

The same speckle pattern application strategy used in tensile testing is also followed for Marciniak testing. To minimize friction between the carrier and the punch, lubrication layers consisting of PTFE foil, high-contact pressure grease, and another layer of PTFE foil are applied to the carrier. The specimen is placed with the speckle pattern facing downward on the lower die's drawbead. The matching carrier is then positioned on top, with the lubrication layers facing the punch. Both the specimen and carrier are aligned in the center of the lower die. The upper die is clamped to the lower die with 20 M10 hex socket cap screws, tightened evenly by alternating sides and using a torque wrench set to 50 Nm. The acquisition time is set on 2 Hz, as the used DIC cameras are not capable of capturing more frames per second. To get sufficient pictures during the whole testing process, the punch velocity is set to 0.25 mm/s. This punch velocity is half of what ISO 12004-2 recommends (*ISO-12004-2.Pdf*, 2021) During the test, the first surface mirror is kept clean with a fiber cloth and ammonia-free glass cleaner.

To achieve the desired stress states, seven types of specimens are used, ranging from Type 1.1 to Type 4, as shown in Figure 3.7. The sides of all the specimens are 180mm. The specimen width W , radius R , and washer diameter D vary for each specimen type as listed in Table 1.

Table 1: The used specimen type dimensions of the carrier and the specimen sheets from Figure 3.7 (right).

Type	Width W [mm]	Radius R [mm]	Diameter D [mm]
1.1	18	81	-
1.2	40.4	69.8	-
2.1	90	-	22
2.2	108	-	22
3.1	112.4	33.8	22
3.2	121.4	29.3	28
4	180	-	23.5

Within the DIC software Istra 4D (*Istra 4D*, 2019), points can be set on each picture of the test specimen. The angle needs to be determined with respect to the second principal strain or axis. In general, the crack angle is deemed zero when perpendicular to the first principal strain. (Bai & Wierzbicki (2010), (Hutchinson & Neale, 1978). Along the fracture, 4 points will be set to limit the human factor. The placement of those points along the fracture can be done differently, and has influence on the measured angle. A weighted average method is chosen to limit the human influence and measure the fracture propagation angles.

The picture is taken when the fracture angle begins to propagate. Four points are then placed along the fracture. This allows for the creation of three triangles: one between the first and fourth points, one between the first and third points, and one between the second and fourth points. An imaginary triangle can then be formed by adding a point with the same y-coordinate as the first point and the same x-coordinate as the second point, as illustrated in Figure 4.5. By using these four points along the fracture, three angles can be calculated. Angles between adjacent points are avoided due to the increased measurement error caused by their short distances. The farther apart the points, the more accurately the angle can be measured. As a result, the angle between the first and last point is given more weight. The first point is positioned at the crack initiation location, serving as the origin. The general angles can then be calculated using the formulas in Equations 5.

$$L_{1-2} = \sqrt{(x_2 - x_1)^2 + (y_2 - y_1)^2 + (z_2 - z_1)^2}$$

$$L_{A-2} = y_2 - y_A$$

$$\text{with } y_A = y_1 \quad (5)$$

$$\theta_{1-2} = \sin^{-1}\left(\frac{L_{A-2}}{L_{1-2}}\right)$$

$$\theta_{average} = 0.5 * \theta_{1-4} + 0.25 * \theta_{1-3} + 0.25 * \theta_{2-4}$$

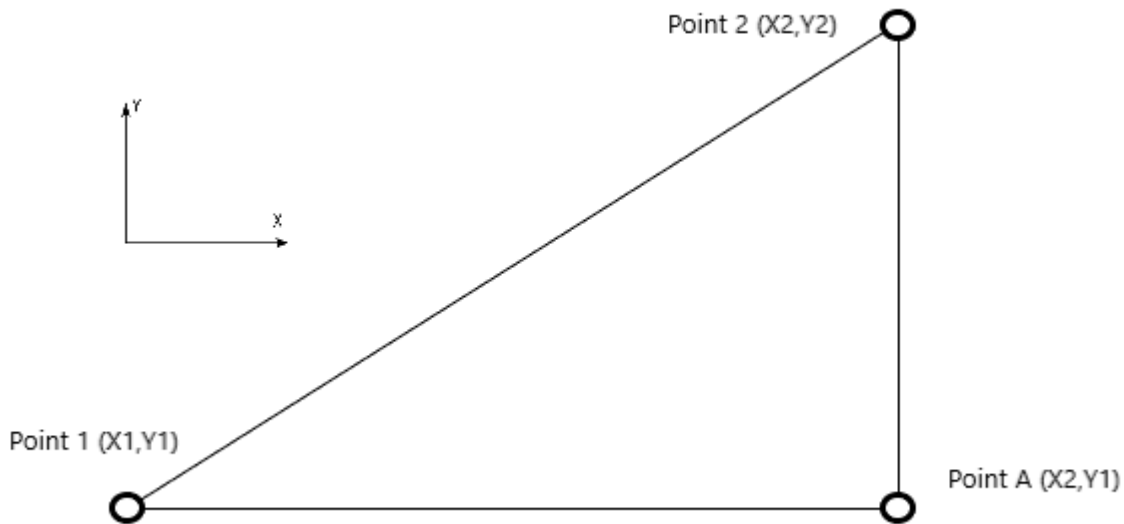


Figure 4.5: The imaginary triangle between 2 points that is used to determine the crack angle.

Using this procedure, the crack angle is determined in the global coordinate system, as represented by the symbol α in Figure 4.6 on the left. Next, this angle needs to be transformed relative to the direction of the second principal strain. The strain tensor values at the origin (point 1) can be obtained from the DIC software Istra 4D (Istra 4D, 2019). By calculating the eigenvectors of the strain tensor, the principal axes are identified. The transformation angle and the required second principal axis are then calculated within the global coordinate system. This transformation angle is denoted by Φ in Figure 4.6 on the right. Depending on the orientation, this transformation angle is either added or subtracted from the determined crack angle α to obtain the crack angle relative to the second principal axis.

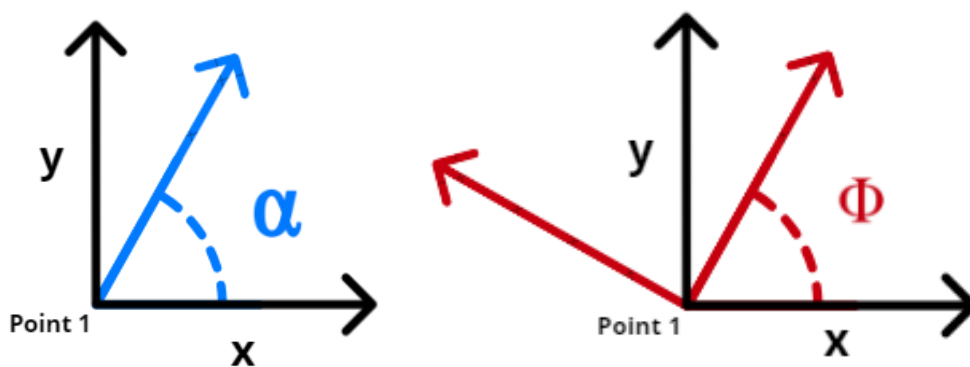


Figure 4.6: The crack angle determination in the global coordinate system (left) and the transformation angle of the global coordinate system to the principal axis system (right).

This procedure is performed in the 2D plane. To ensure its feasibility, the gage section must remain as flat as possible, as shown in Figure 4.7. This guarantees that the global coordinate system, in which the angles are determined, is only translated along the z-direction and does not become tilted. Figure 4.7 illustrates the start (left) and end (right) of the deformation process. In this figure, the origin of the global coordinate system is represented by the red point, while the direction of the x-axis is indicated by the blue point.

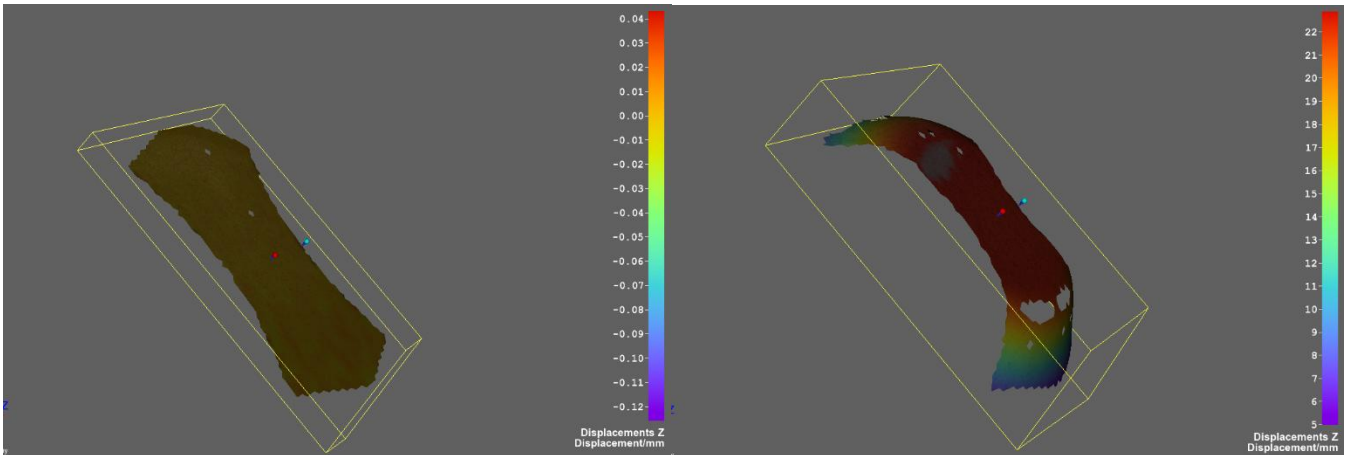


Figure 4.7: The global coordinate system shown at the start (left) and end (right) of the deformation process in the program Istra 4D (*Istra 4D*, 2019). The origin is indicated by the red point and the direction of the x-axis by the blue point.

To determine the FLD, the first and second principal strains are required. By setting a measuring point on the place of initiation of the first fracture, the required principal strains are given by the DIC software. The same procedure as with tensile testing is being used to validate those DIC software results. The coordinate-based method makes it easier to verify if the resulting displacements and strains are reasonable. Additionally, the margin of error of choosing a different principal strain point can also be checked.

The DIC software can also be used to check the requirement that the stress/strain field is evenly distributed over the gage area. The indentation of the specimen should be as homogeneous as possible for all specimen types. The occurrence of necking can also be checked for each test specimen. The difference in the thickness strain in the middle versus at the edge of the gage section shows if the occurrence of necking happens before fracture.

When the width-to-thickness ratio is too low, the relevant crack angle is in the through-thickness direction. The critical width-to-thickness ratio is material-dependent (Hance & Link, 2019). The specimens type 1.1 to 2.2 are therefore cut in half perpendicular to the thickness direction to be able to measure the through-thickness crack angles as well. The width-to-thickness ratio of the other specimen types are deemed big enough. To measure the through-thickness direction crack angle a microscope is used with the software MikroCamLab2 (*MicroCamLab2*, 2012). Figure 4.8 shows an example how a crack angle is measured in the through-thickness direction in MikroCamLab2. The angle is measured with respect to the base of the material. Two angles can be measured this way. The upper crack angle is the necking angle and the lower crack angle is the relevant angle. For this thesis is the bigger crack angle important. The microscope pictures of specimen type 1.1 to 2.2 can be seen in the Appendix.

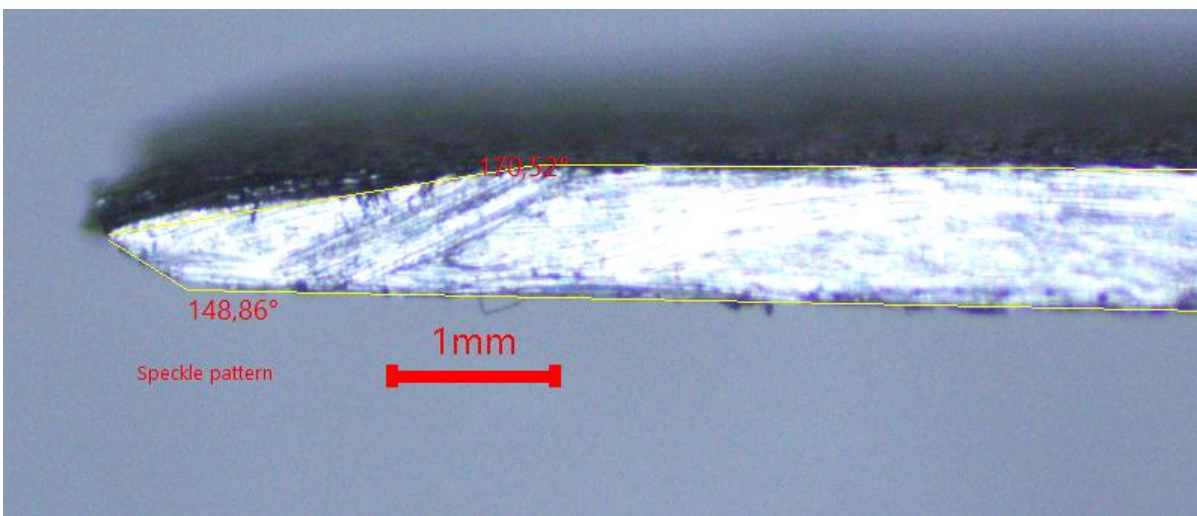


Figure 4.8: The through-thickness angle measurement of Type 2.1 (ρ - ratio = -0.4) in MikroCamLab2 (*MicroCamLab2*, 2012).

5 Results

The main goal was to find the crack orientation for the relevant stress states. Along the way, the DC01 material properties had to be found with tensile testing before the Marciniak testing. Here the results are systematically given starting with the tensile test results.

In Figure 5.1 the determined Lankford parameters are plotted against the angle with respect to the rolling direction. The determination of the Lankford parameter is shown in the Figures 5.2 below. The different repetitions of each specimen are indicated by the V of version, and some repetitions have 2 width strains determined on each side of the crack indicated by S of side.

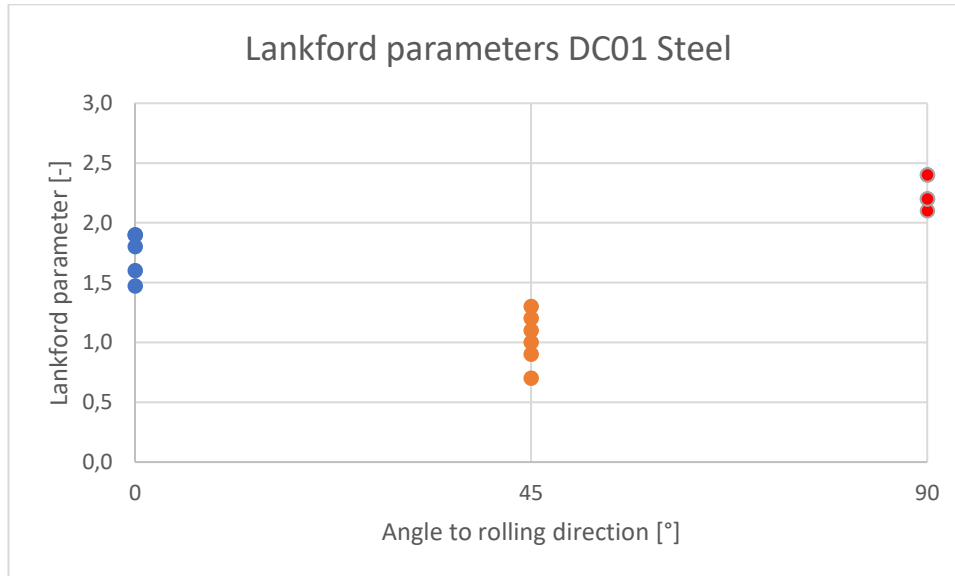


Figure 5.1: The Lankford parameters of DC01 steel plotted against the angles with respect to the rolling direction.

The average Lankford parameters of the DC01 material are determined and listed in Table 2:

Table 2: The determined Lankford parameters of DC01 steel.

Lankford parameters	
r_0	1.7
r_{45}	1.0
r_{90}	2.2

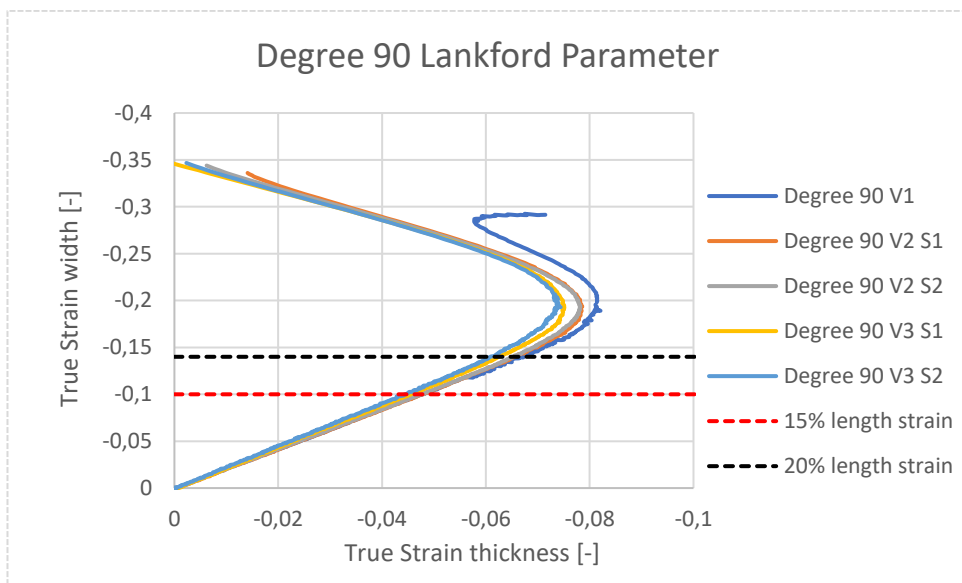
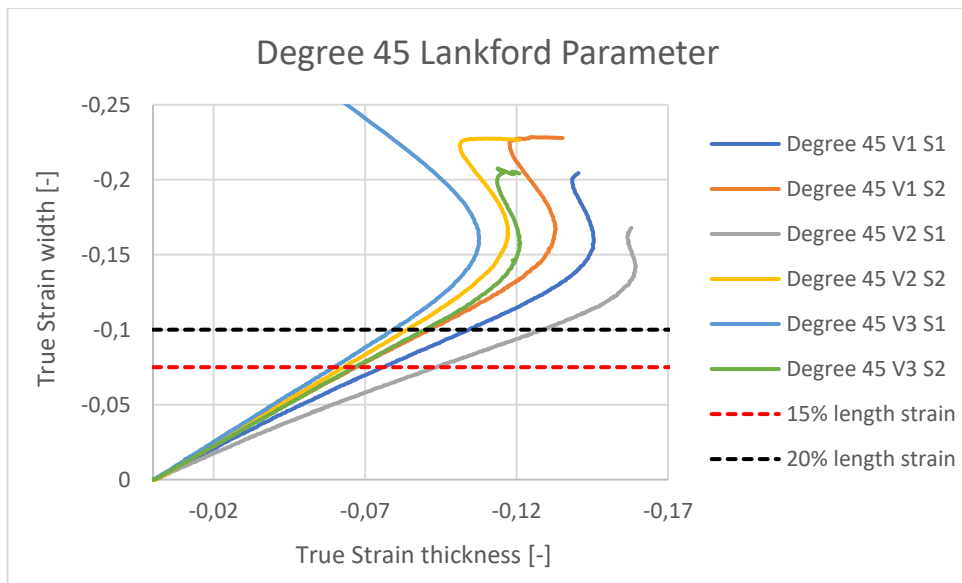
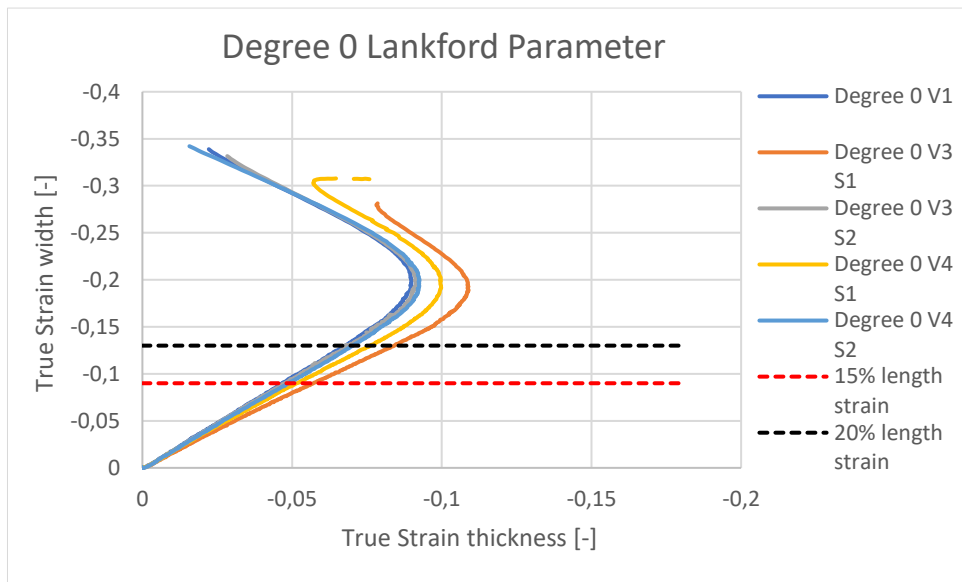


Figure 5.2: The plots of the True strain width vs True strain thickness of each orientation and the 15% to 20% length strain range shown with the dashed lines

The Fracture Limit Diagram of the DC01 steel material can be determined with the Marciniak tests and the DIC. The FLD is shown below in Figure 5.3. The true principal strains measured by the DIC software of the point where the crack initiates are taken. The FLD shows almost linear strain ratios until just before the fracture occurs. The linear strain ratios in the FLD show that the most relevant axial stress states of this project are tested. From the strain ratio of near -0.5 for uni-axial tension of T1,1 to the strain ratio of near 1 for equi-biaxial tension of T4.

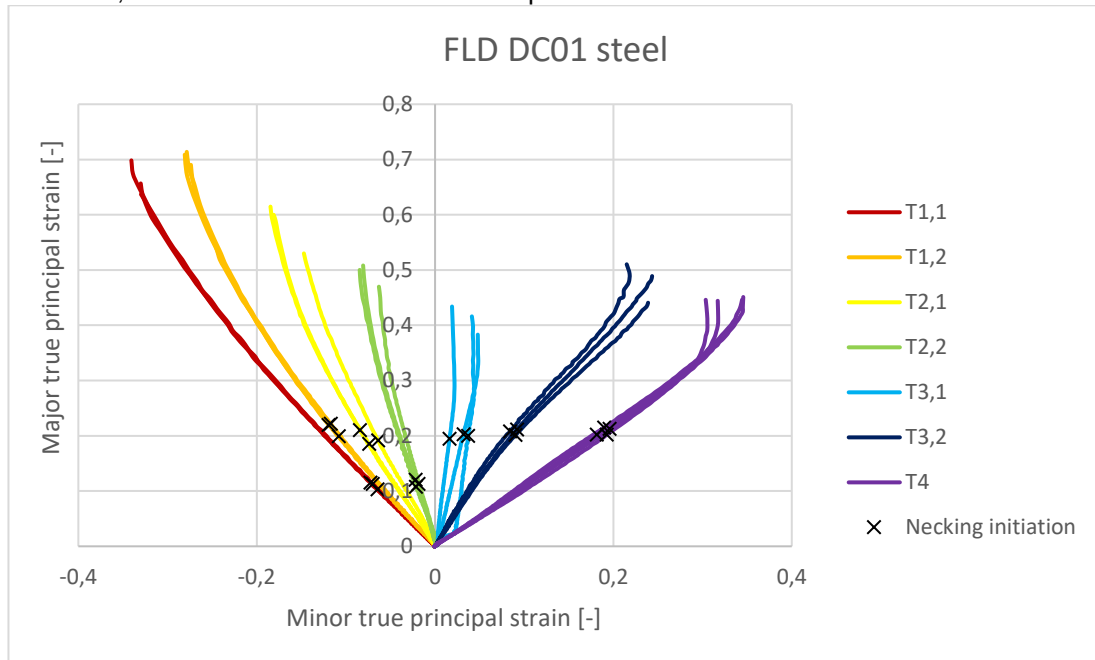


Figure 5.3: The FLD of 1 mm thick DC01 steel material determined using a Marciniak test.

The major true principal strain axes together with the failure crack of all specimen types are shown in Figures 5.4. Apart from Type 4, all the major true principal strain axes are perpendicular to the rolling direction. Only in the case of Type 4 do the axis change significantly.

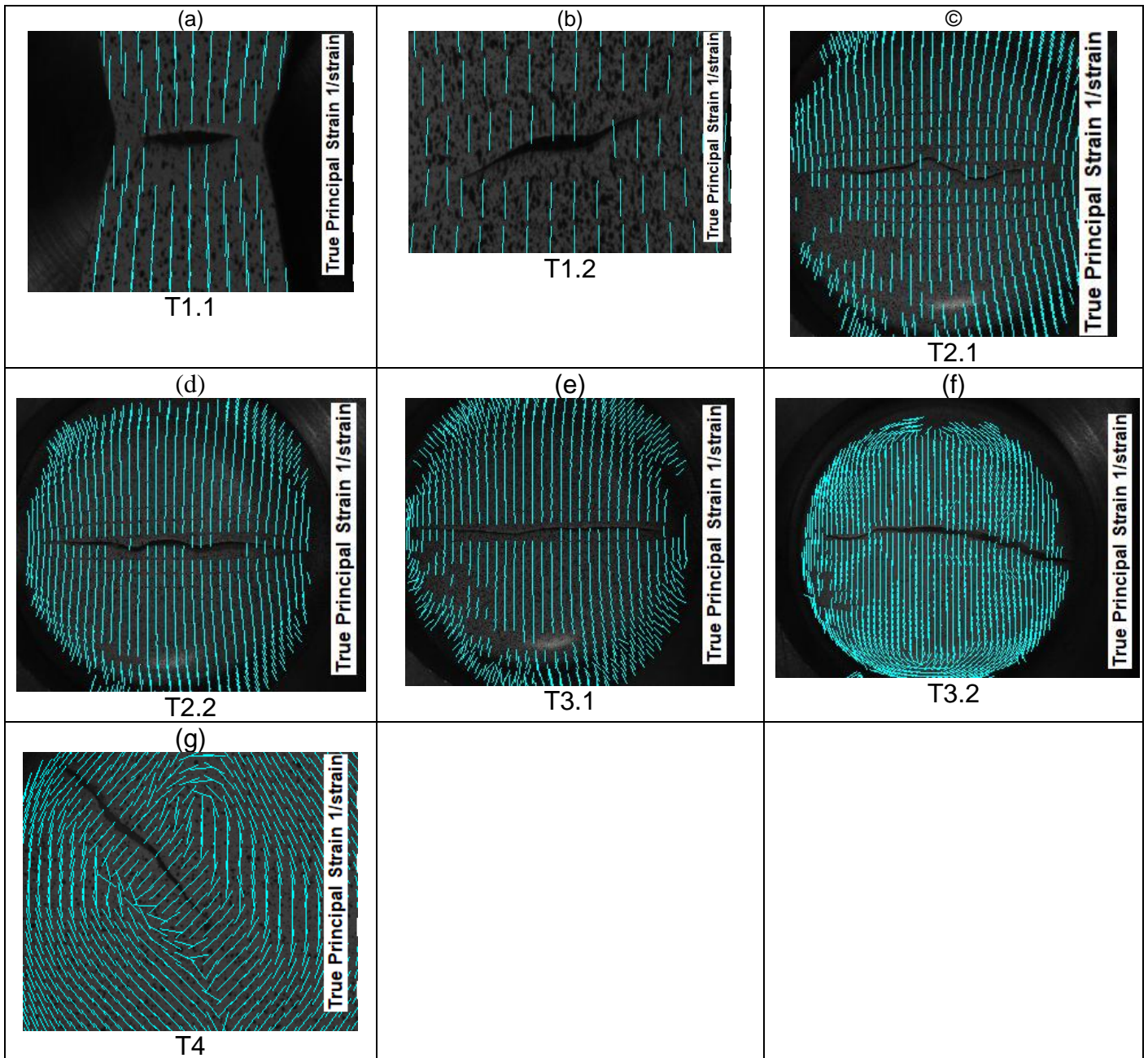


Figure 5.4: The failure cracks of each type are shown with the major true principal strain axis.

The different placement of the points along the fracture of T4V4 can be seen in Figure 5.5. Two distinctive angles can be determined here of the same crack, and resulting in a difference of 10° . Choosing different points along the crack for the principal axis determination resulted in a difference of 3° .

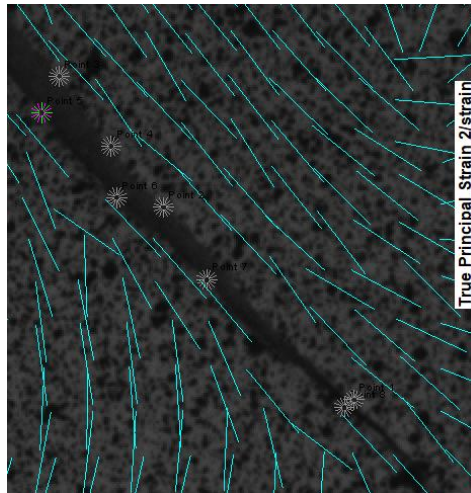


Figure 5.5: The different assigned points along the fracture of repetition T4V4 in the Istra 4D software (*Istra 4D*, 2019).

All crack angles are determined and plotted with respect to the ρ – ratio in Figure 5.6 below. The theoretical angle from the estimation of Hill (1952) is added, from Equation 2. The through-thickness angles measured with the microscope are highlighted in red and the in-plane measured angles with the DIC cameras are highlighted in green. From left to right, groups of points are visible above each other near the same ρ – ratio. Each group of points represents a type of specimen, with most left Type 1.1 and most right Type 4.

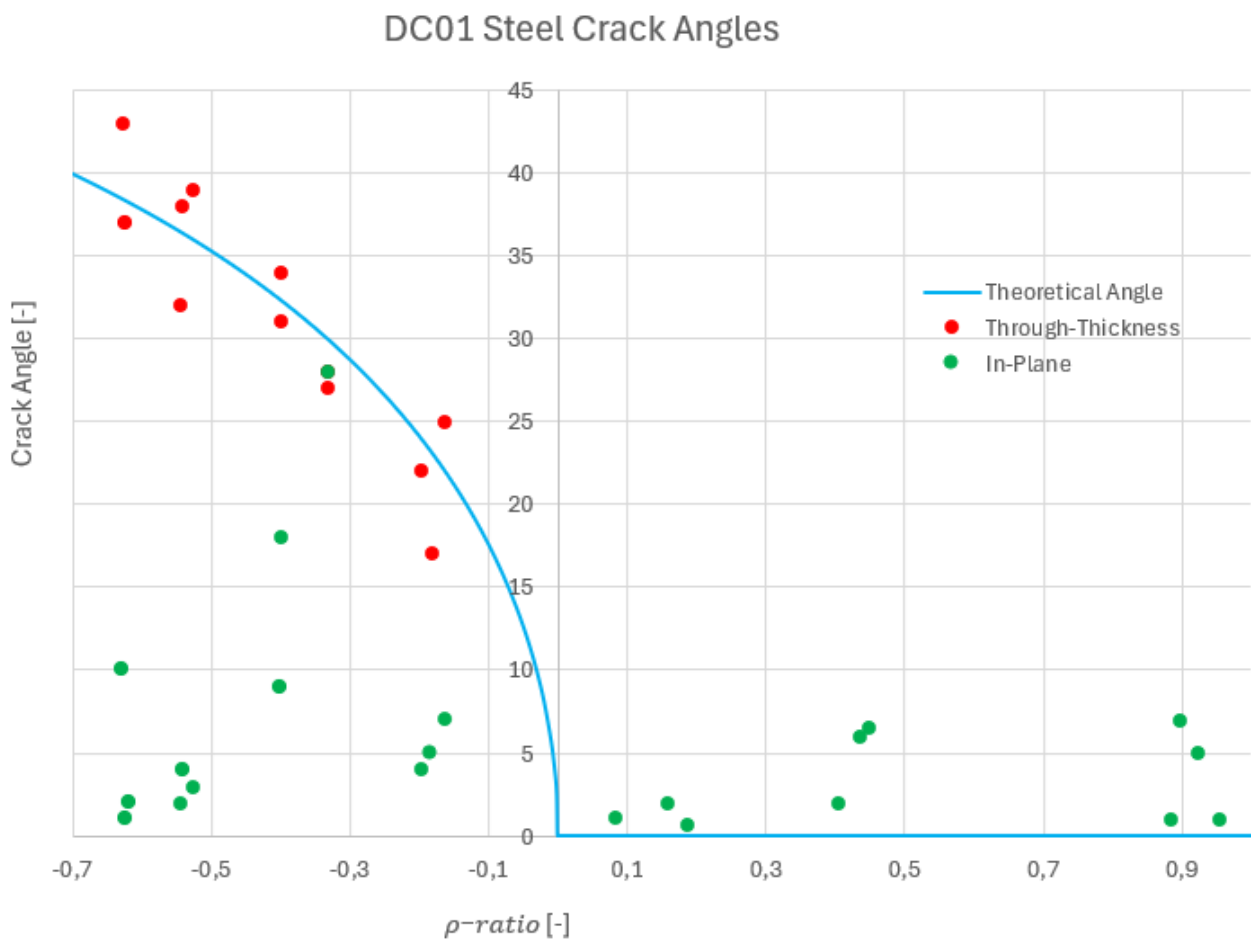


Figure 5.6: The measured crack angles vs the ρ – ratio of 1 mm thick DC01 steel with in red the measured crack angles in the through-thickness orientation and in green measured in the in-plane orientation.

The other requirement of the setup of an even stress/strain field in the gage section is checked in the following Figures 5.7 for specimen Type 4. The first two Figures show the first and second principal stress scaled around the gage section. The three pictures of Figure 5.7 are taken a couple of seconds before failure. The third figure is the z-displacement, the same as the indentation of the specimen, scaled around the gage section. The z-displacement at failure is given for each specimen with the starting location of the crack in the gage section in the Appendix. The z-displacement differences are within 1 mm over the whole gage section, and mostly even within 0.5 mm. The whole gage section for all specimen types is therefore homogeneously displaced with an even stress/strain field.

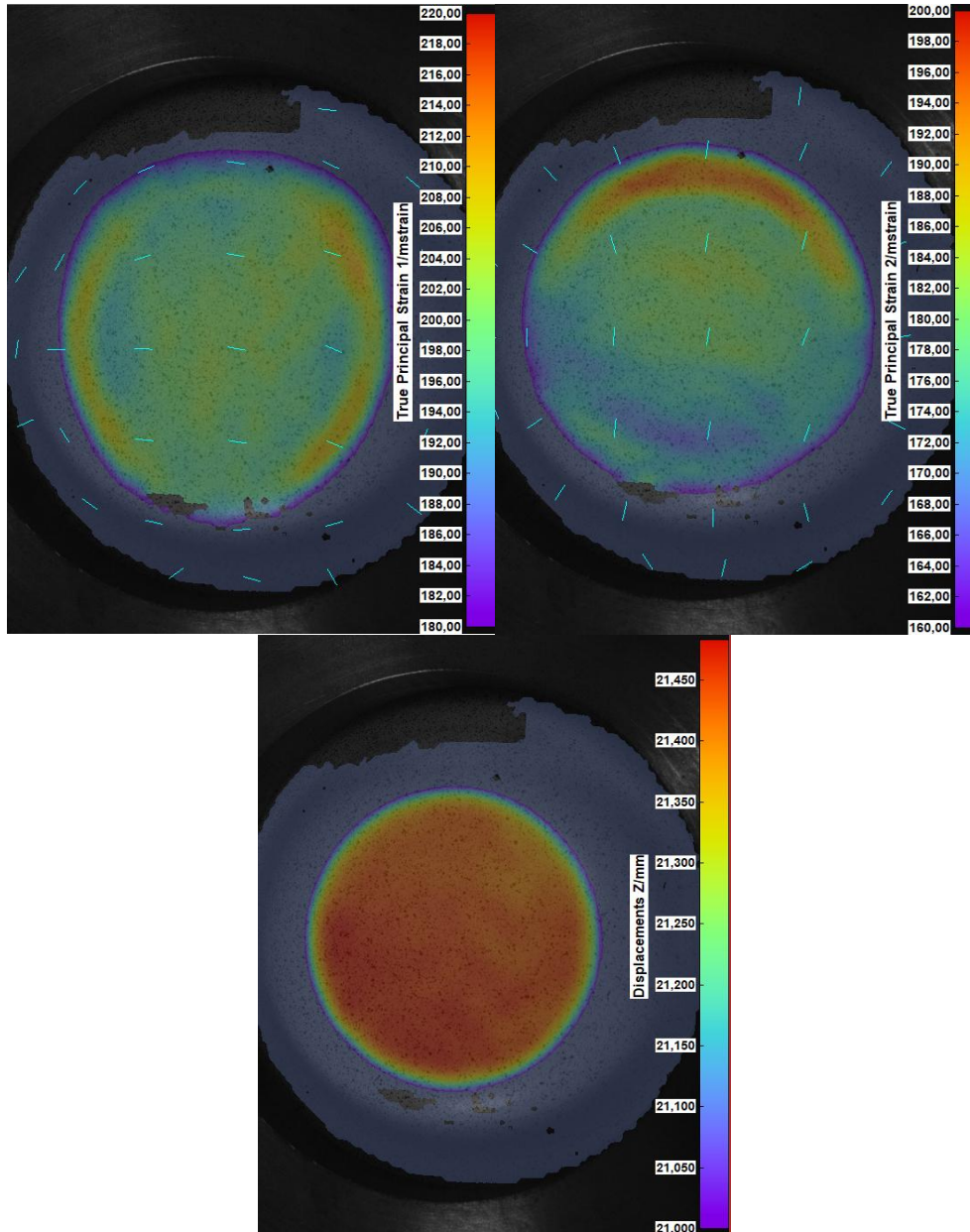


Figure 5.7: Consecutively the true first principal strain field, true second principal strain field, and the z-displacement of specimen T4V4 a couple of seconds before fracture.

Near failure, necking can occur, and this is checked in Figures 5.8, 5.9 and 5.10 by plotting the thickness strain difference at the middle versus at the edge of the gage section. In Figure 5.8, a picture just before fracture is shown with the first true principal strain shown. Three sets of points can be seen. The most left set of points is where the crack initiates, and is used for the FLD. The set of points in the middle above is used for determining the middle strain thickness. The set of points in the middle below is used for determining the strain thickness at the edge of the gage section away from the local strain localization.

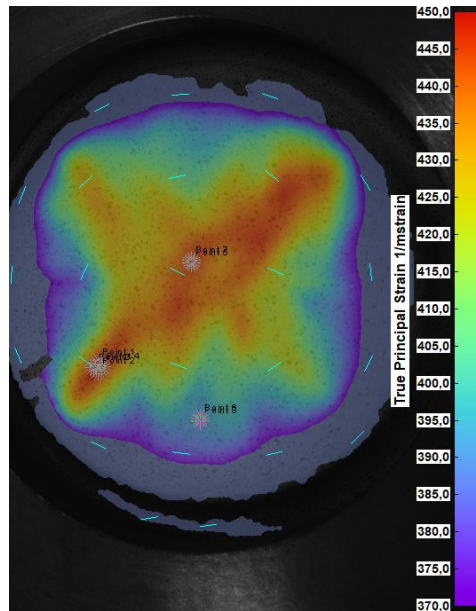


Figure 5.8: A picture of the True principal strain of T4V4 a couple of pictures before fracture showing the local strain fields related to necking.

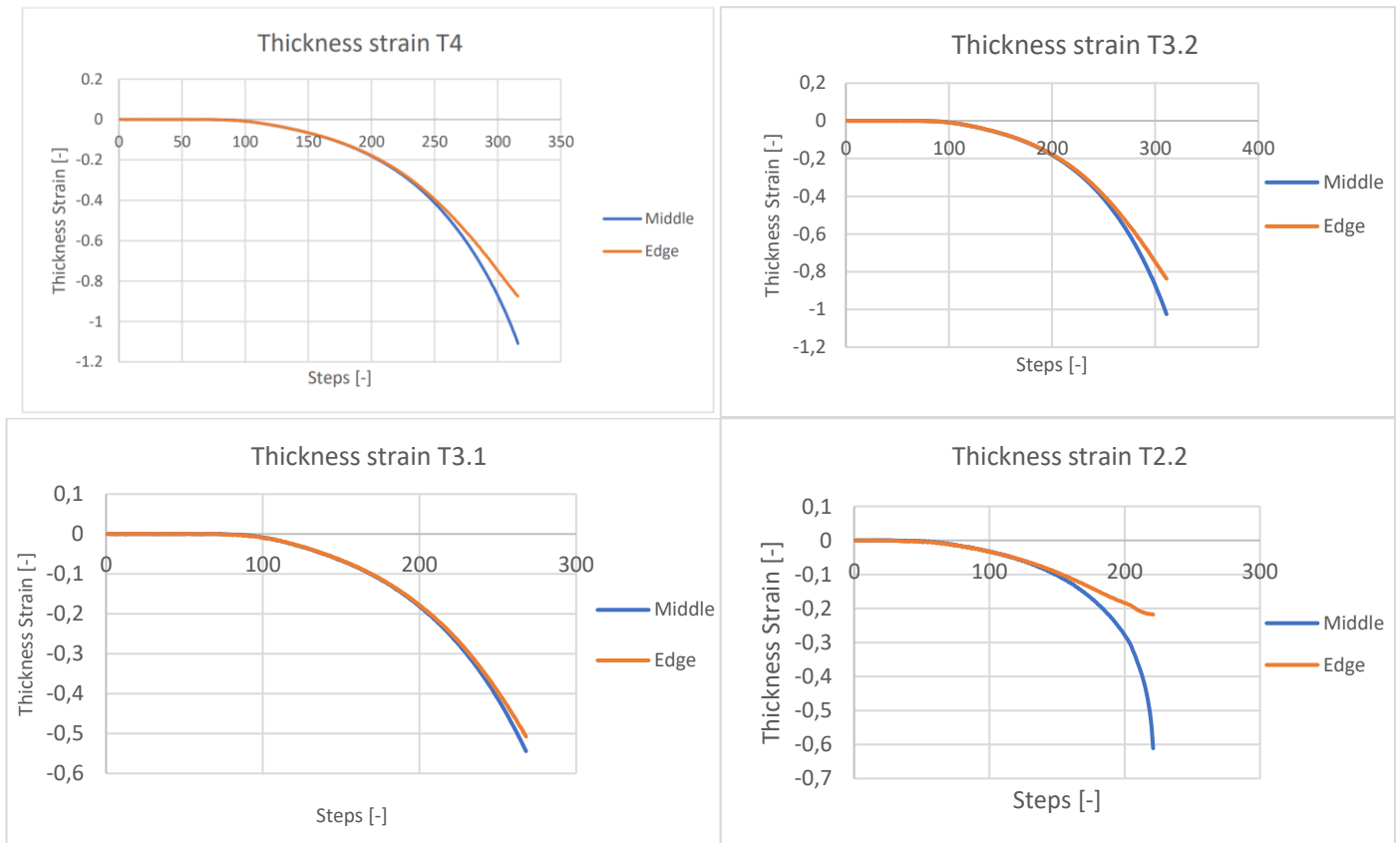


Figure 5.9: The thickness strain of each step of specimen Types T4, T3.2, T3.1 and T2.2 of the middle and the edge of the gage section from which the occurrence of necking can be checked.

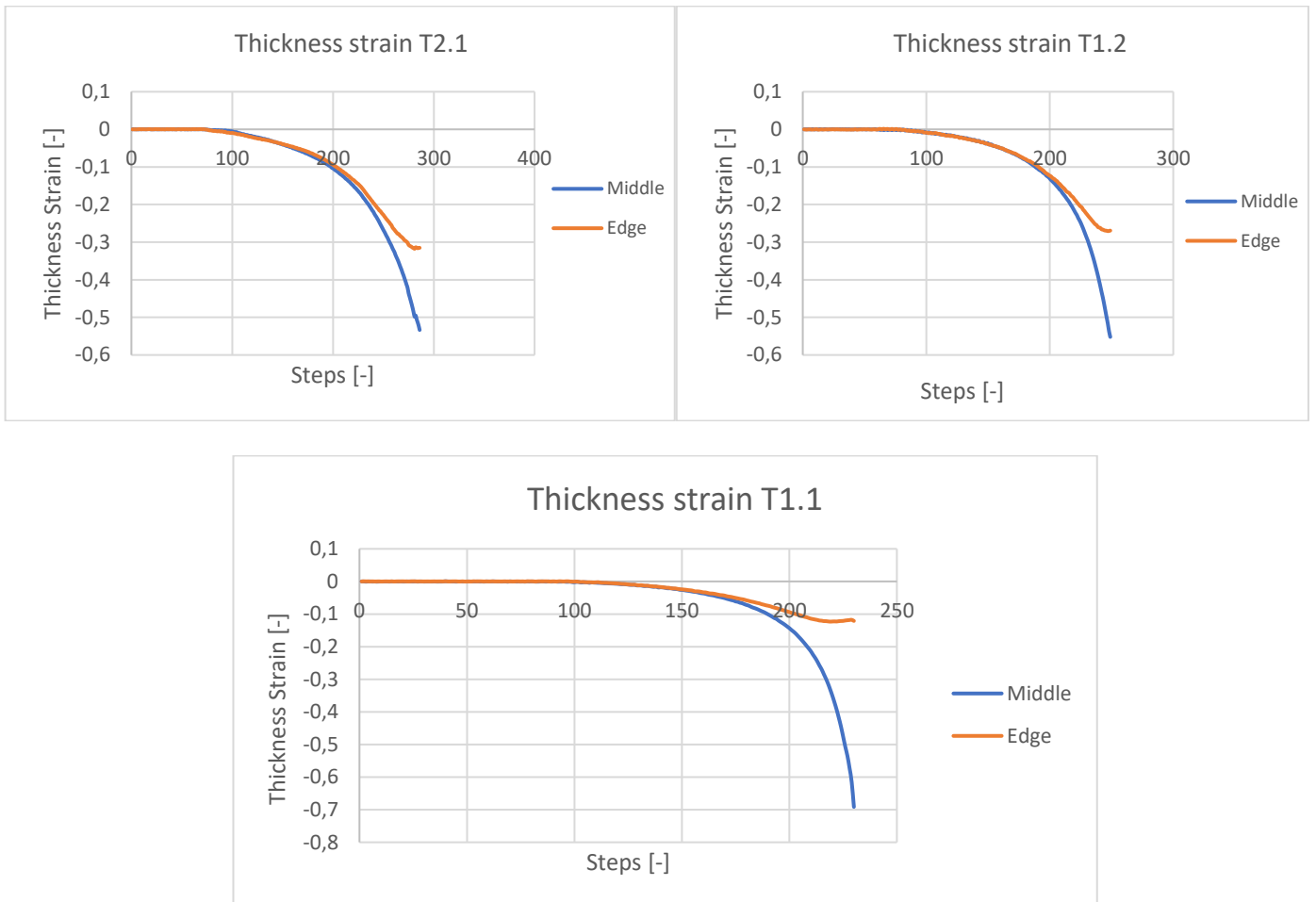


Figure 5.10: The thickness strain of each step of specimen Types T2.1, T1.2 and T1.1 of the middle and the edge of the gage section from which the occurrence of necking can be checked.

All specimen types do show differences in thickness strain. Types 1.1 to 2.2 show a significant change in thickness strain. Type 3.1 has only a slight difference, and Type 3.2 and 4 have a moderate difference.

6 Discussion

This thesis focused on the crack behavior after failure, resulting in Figure 5.6. Figure 5.6 sets the crack angles against the ρ - ratio. Here the distinction can be made of the crack angles of the seven test specimen types. Specimen Type 1.1 resulted in the crack angles near the ρ - ratio of -0.63. Specimen Type 1.2 near the ρ - ratio of -0.54 and so forth till specimen Type 4 near the ρ - ratio of 0.9. This shows the used specimen types cover the most relevant stress states of uni-axial tension (ρ - ratio = -0.5), plane strain tension (ρ - ratio = 0) and near equi-biaxial (ρ - ratio = 1). It can be seen that the crack angles follow Hill's (1952) estimation when the frame of reference is rotated at the negative ρ - ratios.

When looking at the Lankford parameters of Table 2, no angle of 45° is expected near equi-biaxial as r_{45} is lower than r_0 and r_{90} . Dasappa et al. (2012) concluded if r_{90} is considerably higher than the rest, then the crack angle at equi-biaxial goes to 90°. With a 0.5 difference between r_0 , and r_{90} this is theoretically possible. The experimental tests of near equi-biaxial stress show no indication of going towards 90°. More research with different Lankford parameters is needed at equi-biaxial stress to confirm this theory, and better specify the required difference in Lankford parameter values. The Lankford parameters are compared to earlier research and are roughly the same (Meknassi et al., 2022) (Vasile et al., 2017). The exact values of the Lankford parameters of this project are taken from the average of 3 repetitions. More repetitions could give a more accurate value. The Lankford parameters are also taken from the first batch of DC01 sheet material. More batches of DC01 sheet material were ordered at the same company later in the project. It is assumed to be of the same material. All the tests should be done from the same batch of sheets for optimal results.

Yu et al (2022) researched the crack angle of an aluminum sheet in the Nakajima test which resulted in Figure 3.8. Their crack angles followed the theoretical estimation closely while no frame of reference rotation was necessary. Some outliers are visible, but most of the crack angles are near the theoretical estimation. Almost all crack angles are as expected zero on the right side of the FLD of Yu et al (2022). In this project, some of the crack angles at the right side of the FLD are determined as nonzero, but the crack angles should be taken with an error margin of a couple of degrees. More repetitions of all the specimens could give a more accurate estimation of all the crack angles. As for now, no extreme outliers can be identified.

While Yu et al (2022) used an aluminum material, this research is done with a cold-rolled steel sheet. Rolling a material leads to anisotropy, with stronger mechanical properties in the rolling direction and weaker properties in the through-thickness direction (D. Callister, 2018). This can explain the tendency of the crack to fail in the through-thickness direction.

The determination of the crack angle is only feasible if the global coordinate system, where the crack is measured in, is not tilted during the deformation process. The gage section of the test specimens should deform as homogeneously as possible. In Figure 5.7 and in the Appendix, the deformed plane is shown at the initiation of fracture for each specimen type. The difference over the whole gage section for all test specimens is at a maximum of 1mm, and often much lower. This proves the condition of the gage section deforming as homogeneous as possible, and making the angle determination method valid. The value of the determined crack angle must be taken with an error margin of a couple degrees though. The points along the crack are arbitrarily chosen by hand, and can be placed differently as can be seen in Figure 5.5.

Four points are taken along the crack for an average estimation of the crack angle, thus lowering the human influence. The crack angle is taken with respect to the principal axis coordinate system of the first point (crack initiation location) along the crack. The principal axis further on the crack could be slightly different, and result in a slightly different crack angle. This however will result only in a 2° difference, along with the possible maximum difference of 10° when placing the points along the crack. When taking into account that the 10° degree placement difference is a deliberate maximum, and the placement is done as accurately as possible in the middle of the crack, a total error margin of 5° should be reasonable.

Another boundary condition for this project is that the stress state should be as constant as possible. Figure 5.3 shows that each specimen type strain path starts linearly, but most finish in a straight vertical line. For most of the process, the stress states are as constant as possible. Type 4 ends only near the initiation of fracture fully vertically, thus ending in a plane strain stress state. Types 1.1 to 2.2 bend a bit vertically earlier in the process. It should be noted that in Figure 5.2 the final 0.1 major true principal strain consists for all specimen types around a maximum of 3% of the deforming process. If a stress state change can have such an impact during only a small portion of the whole deforming process near the initiation of the fracture is questionable.

The feasibility of the developed formality test is demonstrated by comparing the determined FLD with FLDs from previous research. The FLD of Gutierrez et al. (2020) shown in Figure 6.1 on the left shows the same slight curve towards verticality at the ends. Chen & Fang (2018) got the same vertical strain path at the ends of their Nakajima testing results. The resulting strain path tendency to verticality is therefore expected. More research can be done to limit this tendency and to research the effect.

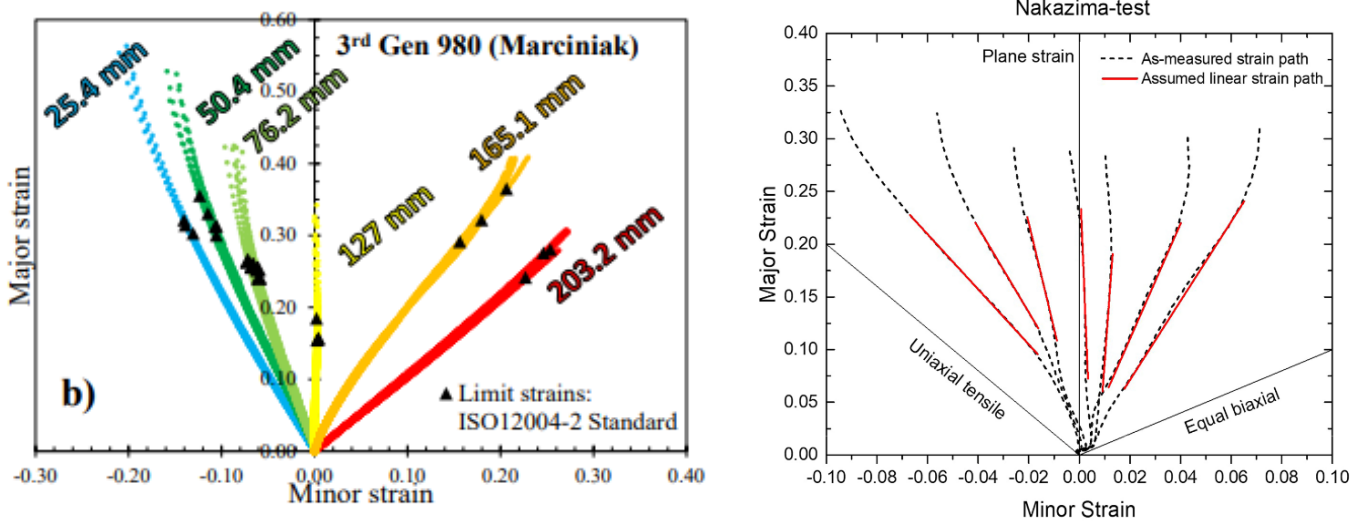


Figure 6.1: A determined FLD of another material using the Marciniak test on the left, and another determined FLD of again another material using the Nakajima test on the right. Both show the tendency of strain paths to go to verticality near the end.

At the start, it was uncertain how much material was needed for all the tests due to the trial and error of the carrier holes for each type. The carrier hole dimension needed to be adjusted for each specimen type while conducting the Marciniak tests to ensure failure in the gage section. A too big carrier hole resulted in a circular failure of the specimen as the edge of the carrier hole cuts into the specimen. Making the carrier hole too small will mostly result in a failure outside the gage section. During testing the carrier often failed before the specimen, which is not optimal. Sometimes the specimen failed outside of the gage section and was therefore dismissed. A more formable carrier material would help reduce this trial and error phase. A more formable carrier can ensure more failures near the middle of the gage section, instead of a few cases where failure happened near the edge of the gage section. If this affects the crack angle is questionable as the stress is as homogeneous as possible in the whole gage section.

In Figures 5.9 and 5.10, the difference in the thickness strain at the middle versus the edge shows if and when the necking initiates. There is no clear value threshold of thickness strain difference that proves if necking occurred or not. Specimen types 1.1 to 2.2 show a significant difference, thus showing that necking has occurred. Type 3.1 shows a small difference, but in the end a 10% difference is visible. At this specimen type necking occurred, but later in the deforming process. Type 3.2 and 4 show also a clear necking initiation. Whether necking happens or not has an effect, but if the significance of the necking has an effect on the crack angle needs to be further researched.

7 Conclusion

In conclusion, this thesis aimed to fill in the knowledge gap of the crack propagation direction for steel materials by answering the following research question:

What is the crack propagation direction for an anisotropic rolled steel for the uni-axial till equi-biaxial tension stress states? And how does this compare with the expected crack angles?

The formability testing method of Marciniak and the different combinations of test specimen and carrier made it possible to determine the crack angle for the relevant stress range: uni-axial to equi-biaxial tension. The measured necking angles of the steel DC01 material agree with the theoretical assumption of Hill (1952) when the frame of reference is rotated at the negative ρ – ratios. Hill's (1952) theoretical assumption applies to the in-plane orientation reference, and Yu et al. (2022) concurred with this assumption for aluminum sheet metal without needing to alter the orientation reference. However, when using cold-rolled steel, the material's tendency to fail first in the through-thickness direction can suggest the need to adjust the reference orientation. Further research on steel that has not undergone the cold rolling process is recommended.

At the positive ρ – ratios a low, but nonzero, crack angle is measured where the crack angle is estimated to be perpendicular to the first principal stress axis, thus a crack angle of zero. At the negative ρ – ratios, the through-thickness orientation crack angles are around the estimated values. In further research, this could be avoided for the positive ρ – ratios if the deformation stops the moment the specimen fails. This way the gage section with the crack remains flat for all specimens, making it easier in post-processing to measure the crack angles in other ways. It should also be noted that all the specimen types neck before failure in this thesis. Some show way more necking than others. The effect of the significance of the necking on the crack angle should be further researched. Through further research, the crack angle in steel sheet metal can be predicted with greater confidence, enabling more accurate simulations and, in turn, improving the assessment of accidental loading conditions.

Further research can avoid some stumble blocks by acknowledging the limitations and recommendations of this research on determining the crack angle for steel sheet material in the Marciniak test. When in further research the Marciniak test is used, a more formable carrier material is advised. More repetitions for each specimen type are also advised to force out the outliers and get a more accurate view of the crack angle for each stress state.

Bibliography

- ASTM E8: Standard & specimens for metals tensile test.* (n.d.). ASTM E8: Standard & Specimens for Metals Tensile Test. Retrieved June 27, 2024, from <https://www.zwickroell.com/industries/metals/metals-standards/metals-tensile-test-astm-e8/>
- Atli-Veltin, B., Dekker, R., Brunner, S. K., & Walters, C. L. (2016). Wrinkling, Fracture, and Necking: The Various Failure Modes in Maritime Crash. *Volume 3: Structures, Safety and Reliability*, V003T02A005. <https://doi.org/10.1115/OMAE2016-54148>
- Bai, Y., & Wierzbicki, T. (2010). Application of extended Mohr–Coulomb criterion to ductile fracture. *International Journal of Fracture*, 161(1), 1–20. <https://doi.org/10.1007/s10704-009-9422-8>
- Banabic, D., Bunge, H.-J., Pöhlandt, K., & Tekkaya, A. E. (2000). *Formability of Metallic Materials* (D. Banabic, Ed.). Springer Berlin Heidelberg. <https://doi.org/10.1007/978-3-662-04013-3>
- Banabic, D., Lazarescu, L., Paraianu, L., Ciobanu, I., Nicodim, I., & Comsa, D. S. (2013). Development of a new procedure for the experimental determination of the Forming Limit Curves. *CIRP Annals*, 62(1), 255–258. <https://doi.org/10.1016/j.cirp.2013.03.051>
- Bong, H. J., Barlat, F., Lee, M.-G., & Ahn, D. C. (2012). The forming limit diagram of ferritic stainless steel sheets: Experiments and modeling. *International Journal of Mechanical Sciences*, 64(1), 1–10. <https://doi.org/10.1016/j.ijmecsci.2012.08.009>
- Chen, Z., & Fang, G. (2018). Determination of forming limit for aluminium alloy sheet eliminating the interferences of through-thickness stress and non-linear strain path. *IOP Conference Series: Materials Science and Engineering*, 418, 012051. <https://doi.org/10.1088/1757-899X/418/1/012051>
- Chung, K., Kim, H., & Lee, C. (2014). Forming limit criterion for ductile anisotropic sheets as a material property and its deformation path insensitivity. Part I: Deformation path insensitive formula based on theoretical models. *International Journal of Plasticity*, 58, 3–34. <https://doi.org/10.1016/j.ijplas.2014.03.009>

- Coppejans, O., & Werter, N. (2022). Discretization Challenges in Crash Simulations: Mesh, Geometry and Failure Criterion Effects From the Energy Perspective. *Volume 2: Structures, Safety, and Reliability*, V002T02A011. <https://doi.org/10.1115/OMAE2022-79655>
- D. Callister. (2018). *Materials science and engineering an introduction* (8th ed.). JOHN WILEY & SONS INC.
- Dasappa, P., Inal, K., & Mishra, R. (2012). The effects of anisotropic yield functions and their material parameters on prediction of forming limit diagrams. *International Journal of Solids and Structures*, 49(25), 3528–3550. <https://doi.org/10.1016/j.ijsolstr.2012.04.021>
- Deng, Z., & McGuire, J. P. (2018). Development of novel forming limit curve testing method. *IOP Conference Series: Materials Science and Engineering*, 418, 012049. <https://doi.org/10.1088/1757-899X/418/1/012049>
- Gutierrez, J. E., Noder, J., & Butcher, C. (2020). Experimental Characterization and Deterministic Prediction of In-Plane Formability of 3rd Generation Advanced High Strength Steels. *Metals*, 10(7), 902. <https://doi.org/10.3390/met10070902>
- Guzmán, C. F. (2015). *Experimental and Numerical Characterization of Damage and Application to Incremental Forming*.
- Hance, B. M., & Link, T. M. (2019). Effects of fracture area measurement method and tension test specimen type on fracture strain values of 980 class AHSS. *IOP Conference Series: Materials Science and Engineering*, 651(1), 012061. <https://doi.org/10.1088/1757-899X/651/1/012061>
- Heidari, H., & Walters, C. L. (2020). State of the Art in Determination of Crack Direction in Shell Structures. *Volume 2A: Structures, Safety, and Reliability*, V02AT02A010. <https://doi.org/10.1115/OMAE2020-18217>
- Hill, R. (1952). On discontinuous plastic states, with special reference to localized necking in thin sheets. *Journal of the Mechanics and Physics of Solids*, 1(1), 19–30. [https://doi.org/10.1016/0022-5096\(52\)90003-3](https://doi.org/10.1016/0022-5096(52)90003-3)

ISO. (n.d.). *ISO 12004-2:2021. International Organization for Standardization.*

[ISO-12004-2-2021.pdf](#)

Istra 4D (Version 4.4.7). (2019). [Computer software]. Dantec Dynamics.

Meknassi, R. F., Béres, G., & Lukács, Z. (2022). Study the near plane strain tensile test specimen using finite element code ABAQUS. *Multidiszciplináris Tudományok*, *12*(3), 107–116.

<https://doi.org/10.35925/j.multi.2022.3.10>

MicroCamLab2. (2012). [Windows]. Meade Instrument Europe.

Moshksar, M. M., & Mansorzadeh, S. (2003). Determination of the forming limit diagram for Al 3105 sheet.

Journal of Materials Processing Technology, *141*(1), 138–142. [https://doi.org/10.1016/S0924-0136\(03\)00262-0](https://doi.org/10.1016/S0924-0136(03)00262-0)

Raghavan, K. S. (1995). A simple technique to generate in-plane forming limit curves and selected applications. *Metallurgical and Materials Transactions A*, *26*(8), 2075–2084.

<https://doi.org/10.1007/BF02670679>

Rigo, P., & Rizzuto, E. (2003). Analysis and Design of Ship Structure. *Ship Design*, *1*.

Tisza, M., & Kovács, Z. P. (2012). New methods for predicting the formability of sheet metals. *Journal of Production Processes and Systems*, *6*, 33–41.

Vasile, R., Racz, S.-G., & Bologa, O. (2017). Experimental and numerical investigations of the steel sheets formability with hydroforming. *MATEC Web of Conferences*, *94*, 02016.

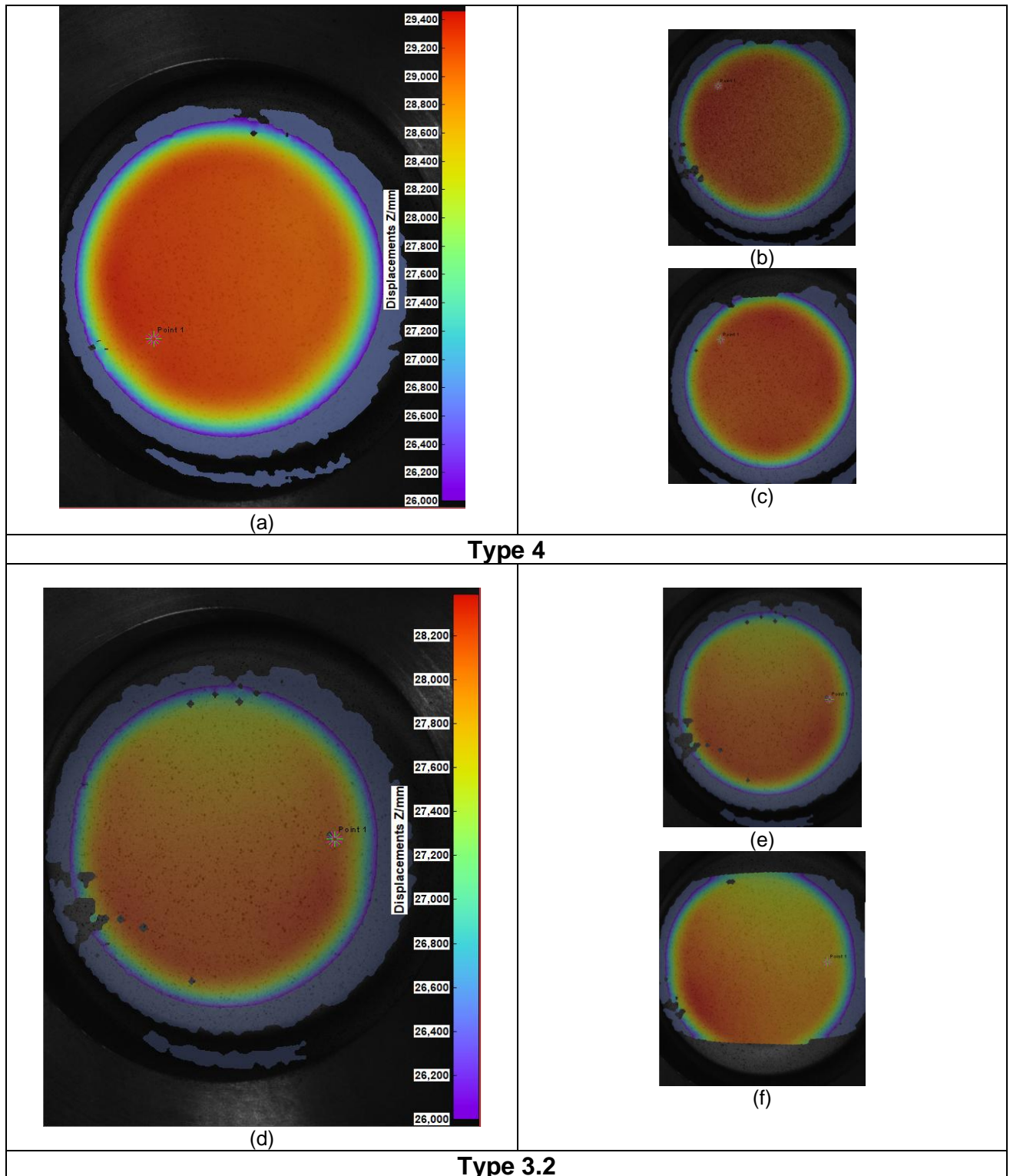
<https://doi.org/10.1051/matecconf/20179402016>

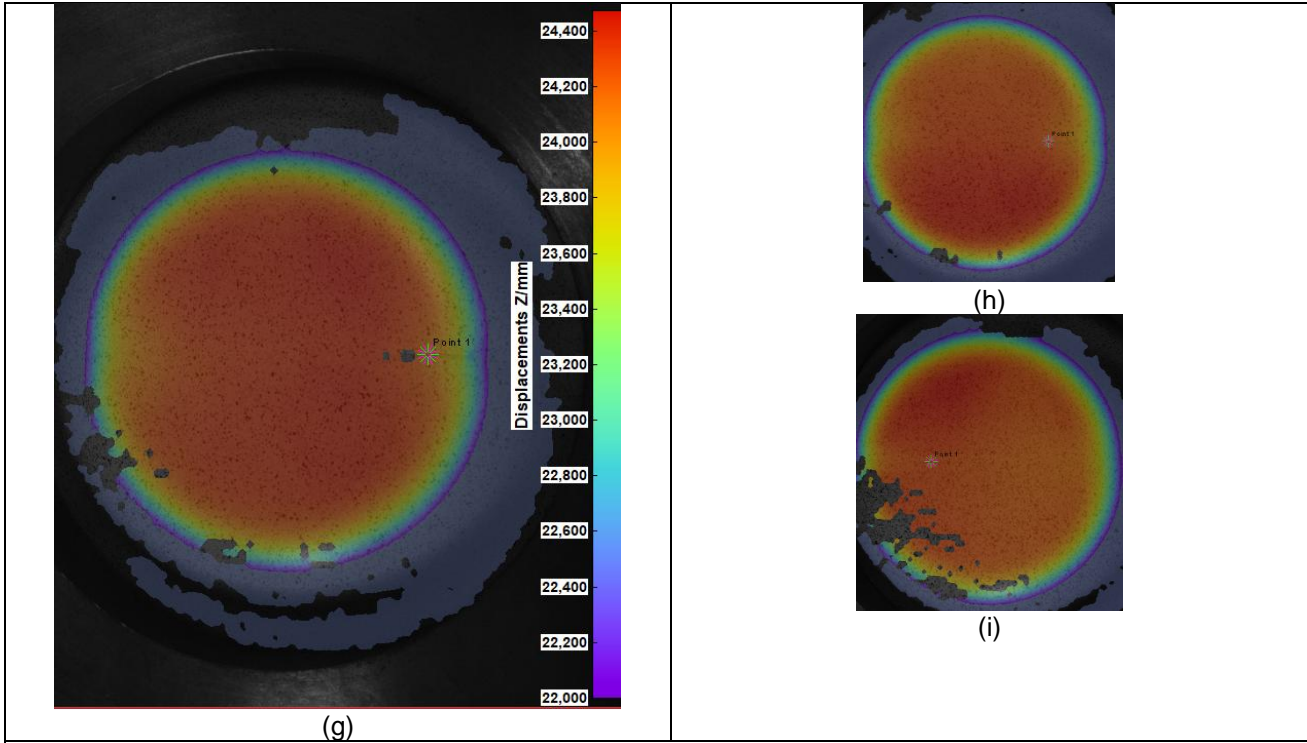
Worldautosteel. (2021, March 23). *R-Value*. AHSS Guidelines. <https://ahssinsights.org/forming/mechanical-properties/r-value/>

Yu, K., Li, Q., Wu, Y., Guo, M., Li, D., Liu, C., Zhuang, L., & Wu, P. (2022). An improved Marciniak-Kuczynski approach for predicting sheet metal formability. *International Journal of Mechanical Sciences*, *221*, 107200. <https://doi.org/10.1016/j.ijmecsci.2022.107200>

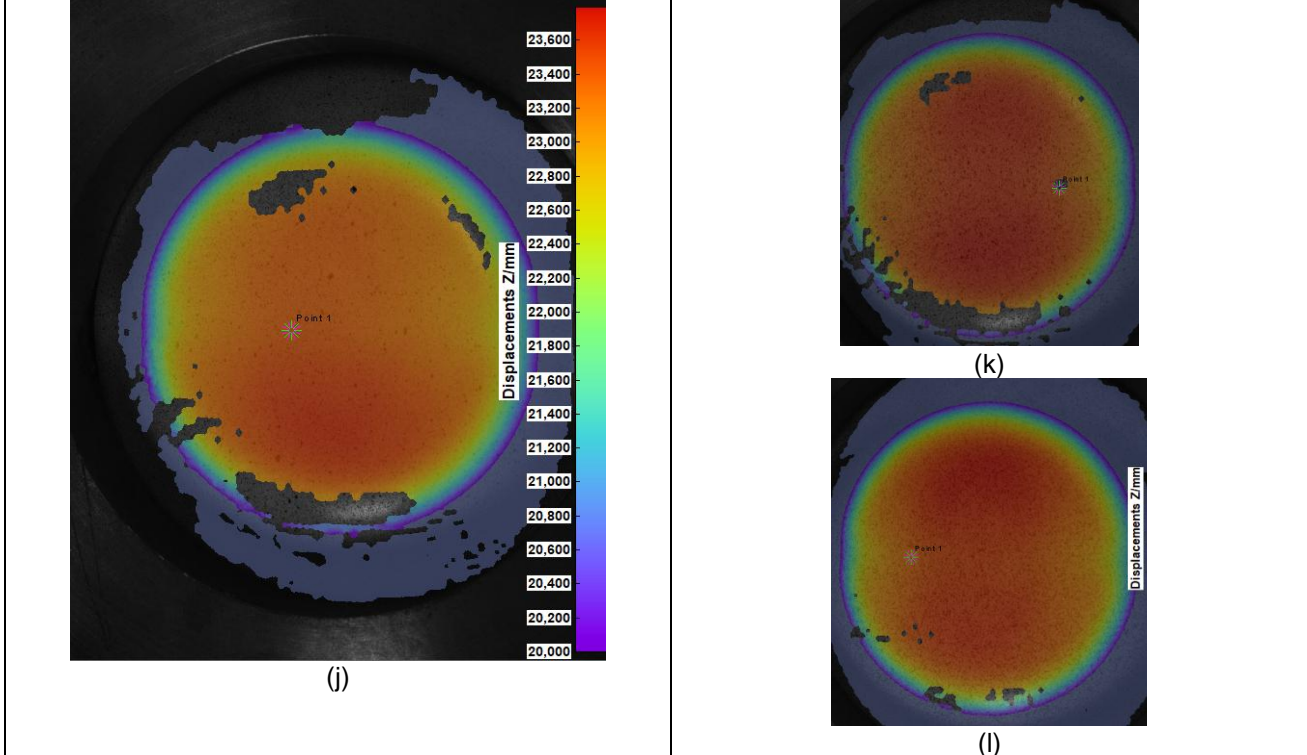
Appendix

The z-displacement of each specimen with the initiation location of the crack given below.

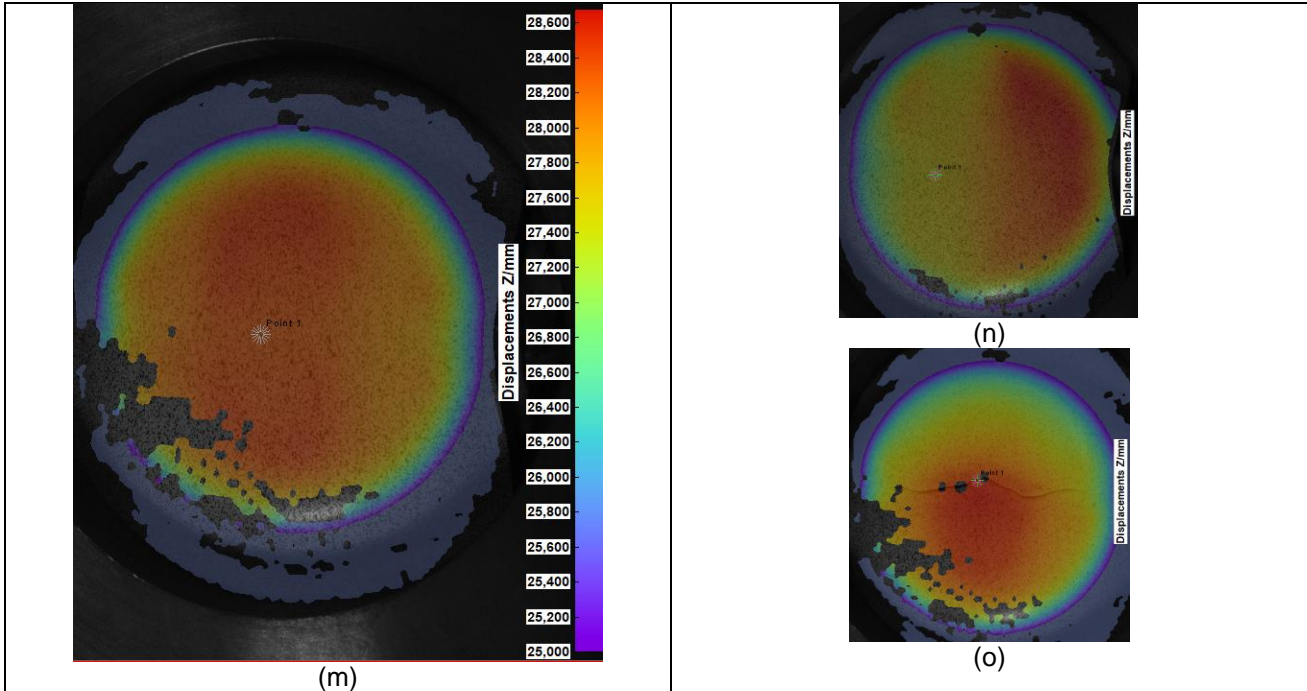




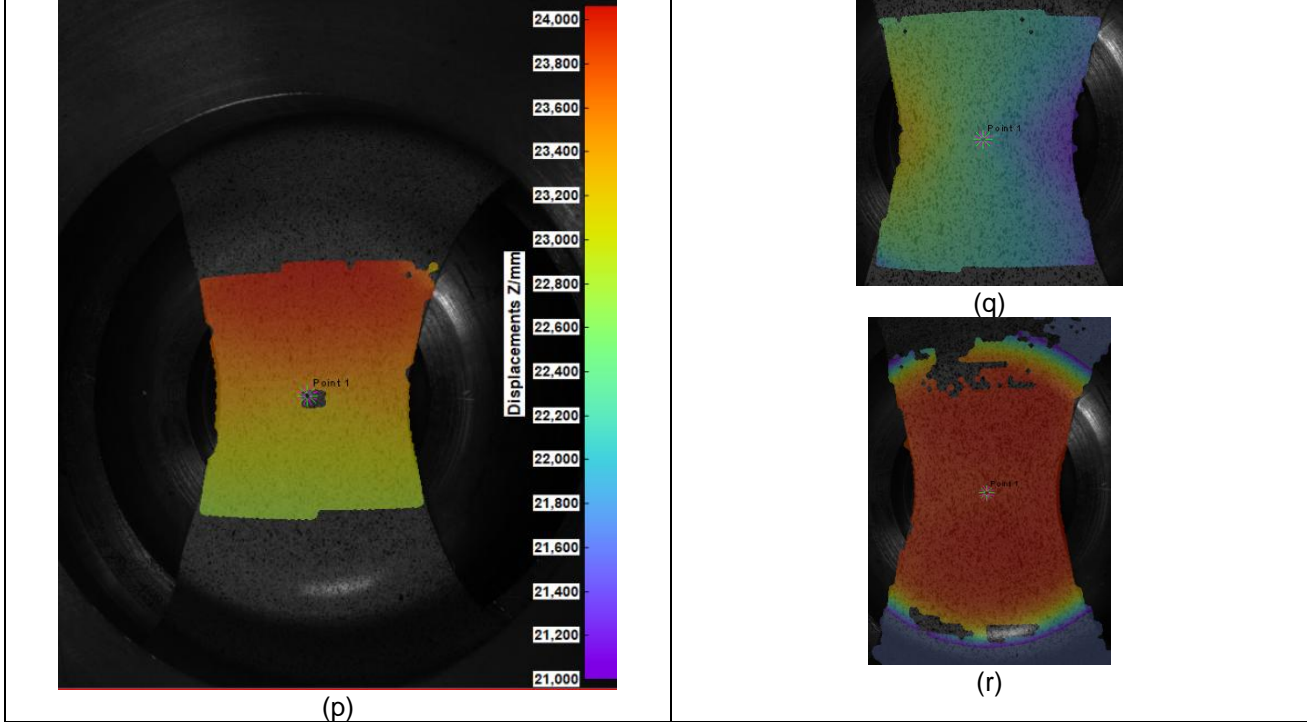
Type 3.1



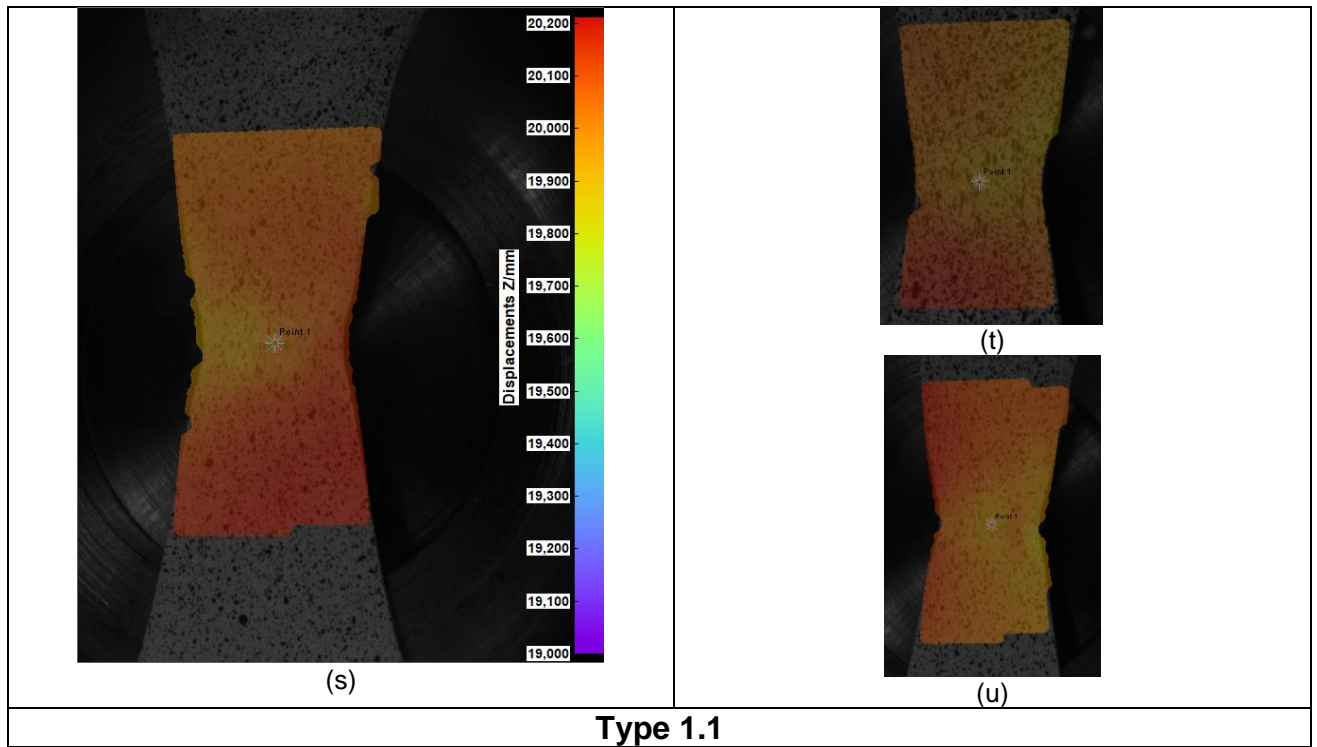
Type 2.2



Type 2.1

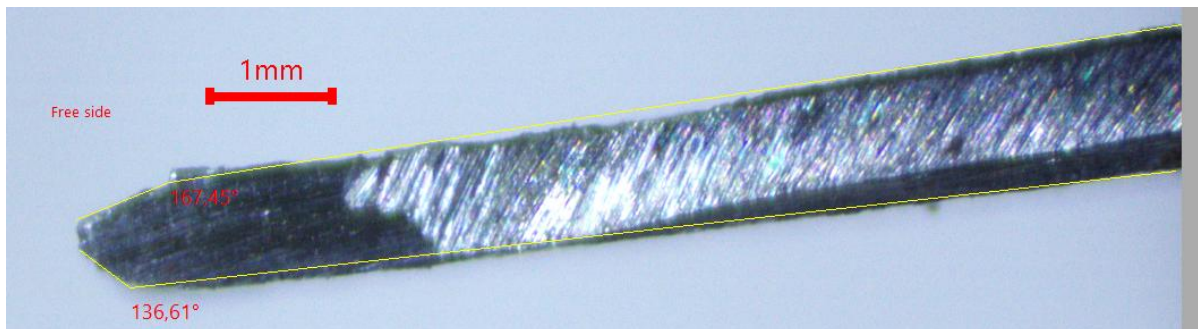


Type 1.2

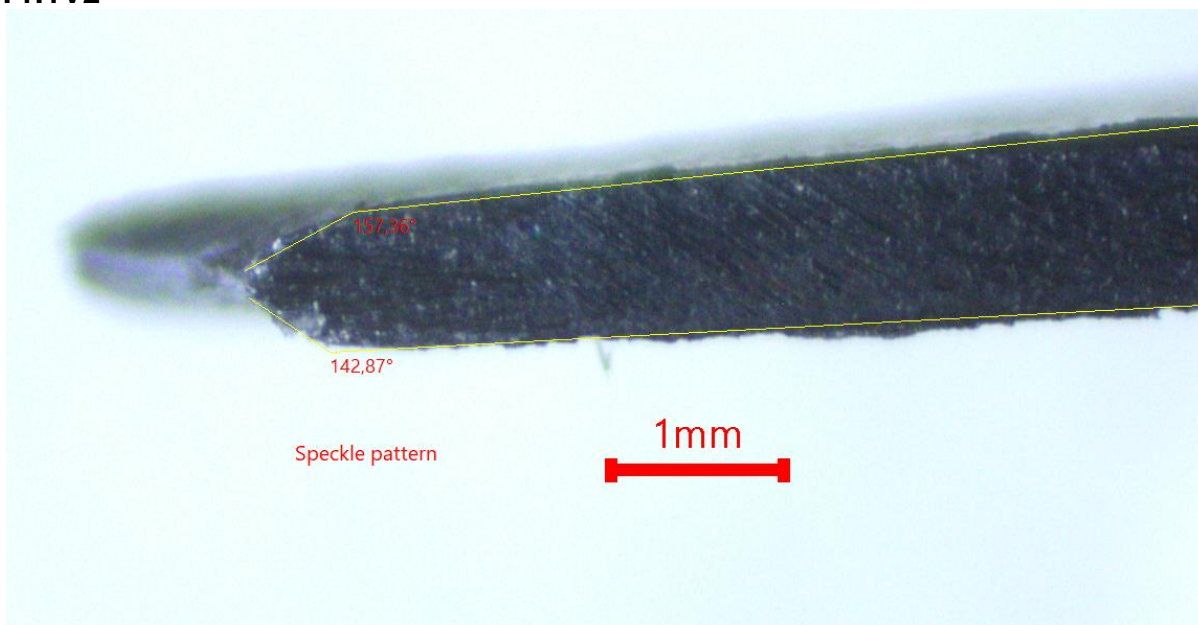


The microscope pictures of specimen types 1.1 to 2.2 from MikroCamLab2 (*MicroCamLab2*, 2012).

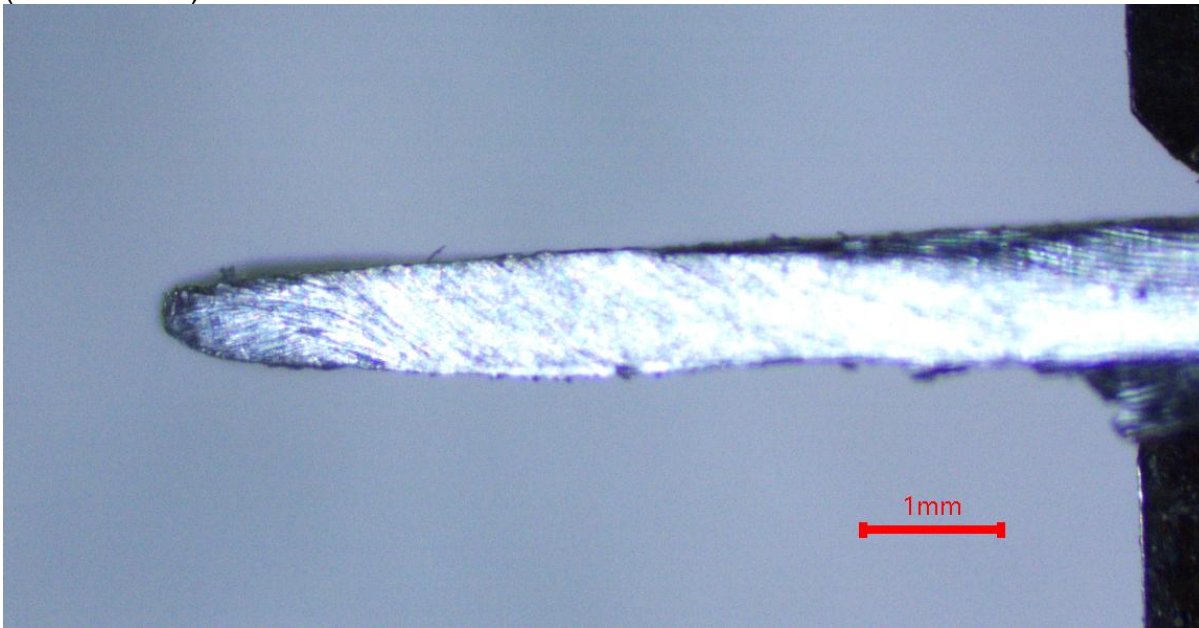
T1.1V1



T1.1V2



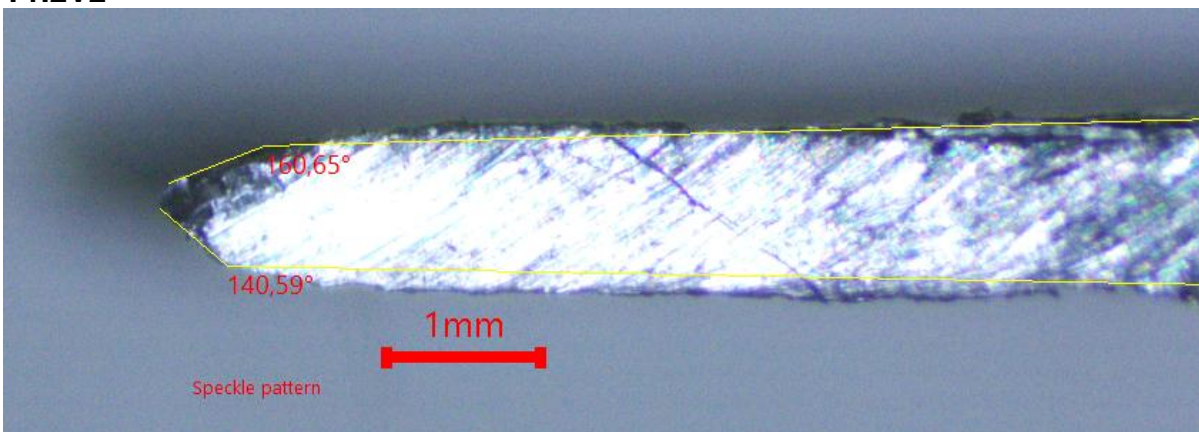
T1.1V3
(Inconclusive)



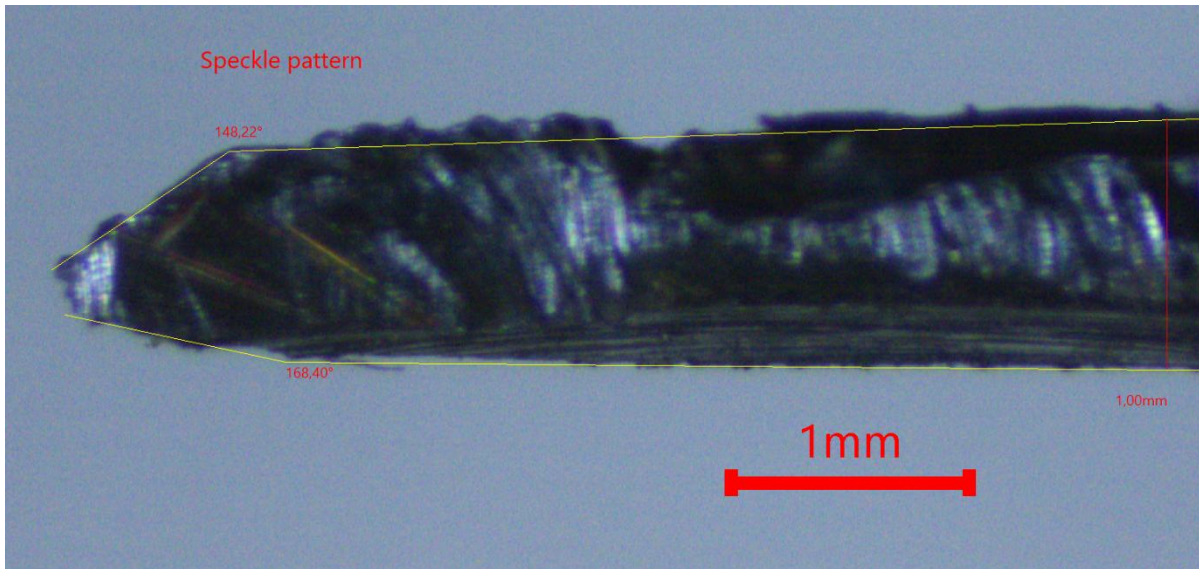
T1.2V1



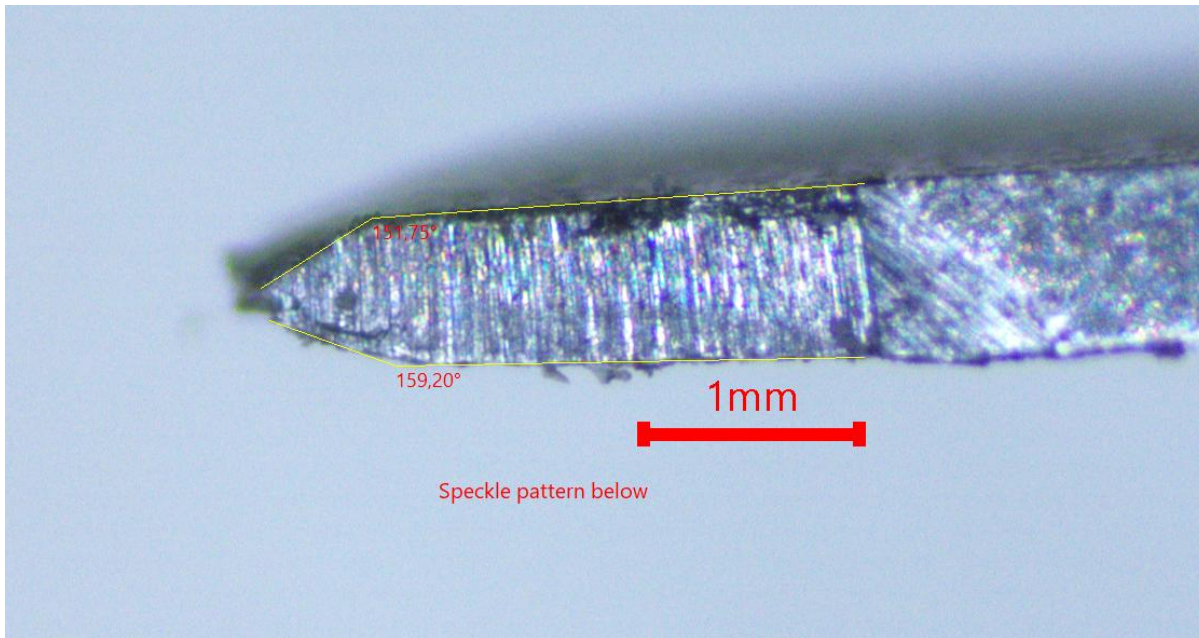
T1.2V2



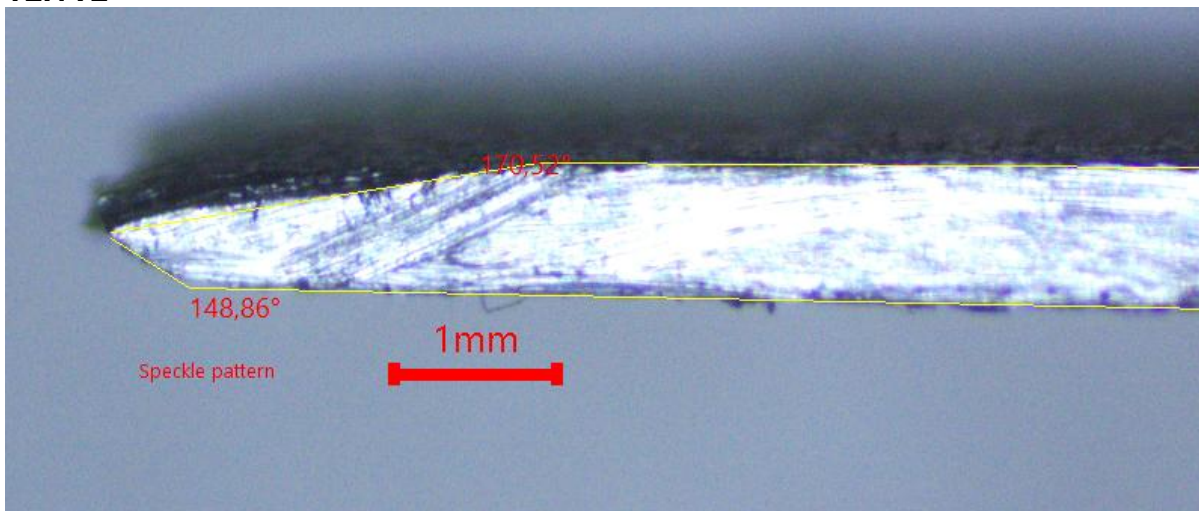
T1.2V3



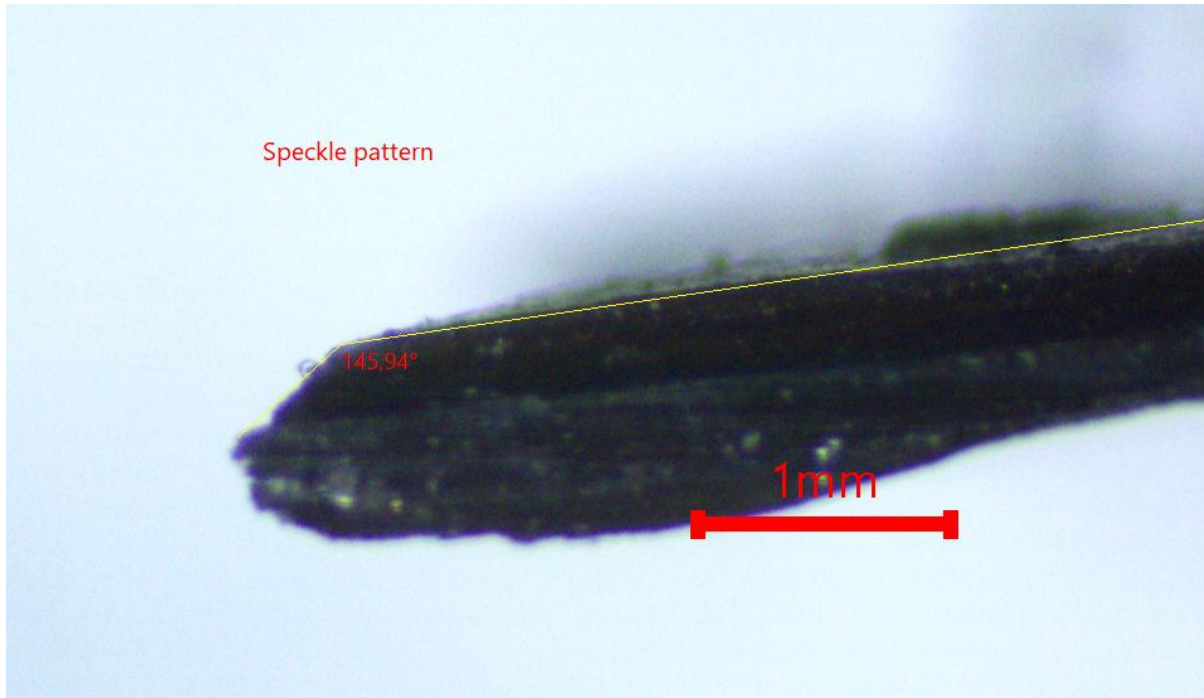
T2.1V1



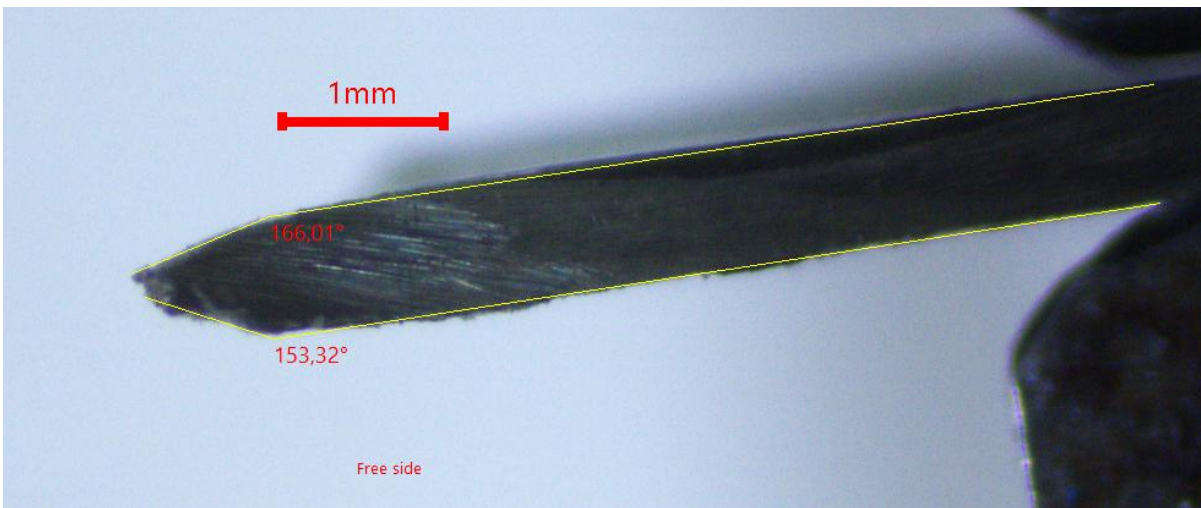
T2.1V2



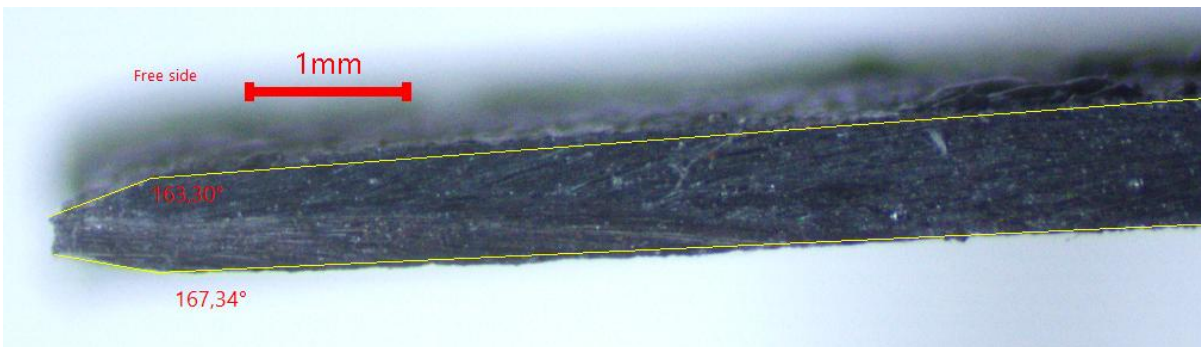
T2.1V3



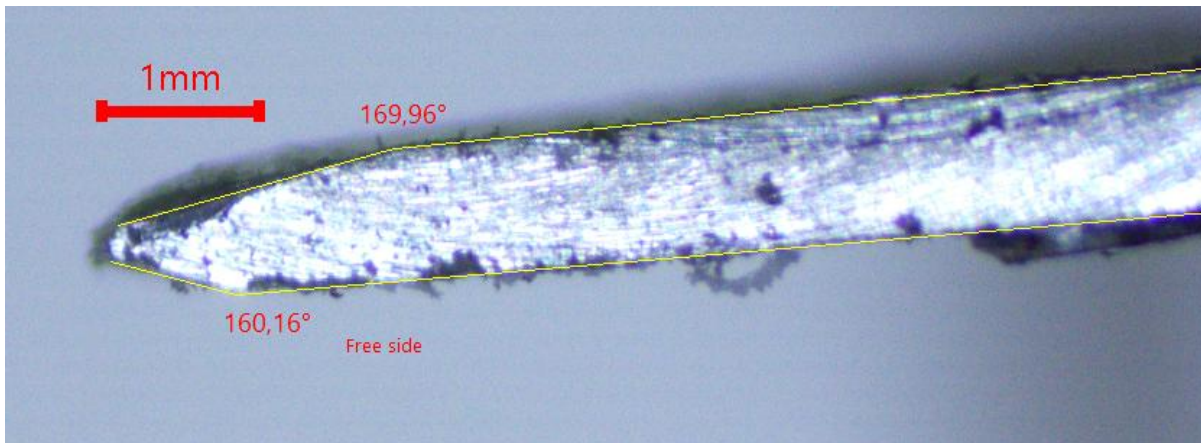
T2.1V4



T2.2V1



T2.2V2



T2.2V3

